Corbino Thermopower of Fractional Quantum Hall States in the Second Landau Level

Frédéric Boivin

A thesis submitted to McGill University in partial fulfillment of the requirements of the degree of

Master of Science

Department of Physics
McGill University
Montréal, Quebec, Canada
August 2025

Abstract

The $\nu = 5/2$ fractional quantum Hall (FQH) has recently been proposed to be a platform enabling topological quantum computations, sparking extensive works aimed at unraveling its many-body wavefunction. To this end, experimentally demonstrating that this exotic state is non-Abelian is a crucial milestone to achieve fault-tolerant quantum computations. Among many others, one promising avenue is to probe the entropy *via* thermopower at a temperature where dimensional entropy dominates, hence providing compelling evidence for its non-Abelian nature.

In this thesis, an ultra-high electron mobility Corbino device was adapted to allow for thermopower measurements in the second Landau level (SLL) of the fractional quantum Hall effect (FQHE) at temperatures of a few milli-Kelvins. In this configuration, low-frequency thermoelectricity was generated with a micrometer-sized chip resistor heater creating a time-varying temperature gradient. Inspired by previous experiments in the Hall bar geometry, a method was implemented to calibrate the temperature gradient *in-situ* in the Corbino geometry. As a result, thermoelectric voltages were converted to thermopower in order to compare longitudinal diffusion Corbino thermopower results with theoretical expectations. A clear observation of non-Abelian entropy *via* Corbino thermopower was hindered by an unexpected deterioration of the $\nu = 5/2$ fractional quantum Hall (FQH) state caused by the chip resistor heater. Nonetheless, based on multiple experimental validations and comparison with earlier works in the Corbino geometry, the voltages probed with this setup were established to be genuine thermoelectric signals and constitute, to our knowledge, a first instance in the literature of Corbino thermopower in the SLL of the FQHE.

Abrégé

Une proposition théorique récente impliquant que l'état quantique 5/2 de l'effet Hall quantique fractionnaire pourrait être utilisé pour concevoir des qubits topologiques a propulsé la communauté scientifique à étudier l'origine physique de sa fonction d'onde. Dans cette optique, obtenir une preuve expérimentale de son comportement non-Abélien prédit par la théorie est une étape primordiale pour implémenter le calcul quantique protégé topologiquement. Parmi plusieurs possibilités, une mesure de l'entropie par le biais de l'effet thermoélectrique dans un régime de température dominé par l'entropie dimensionnelle constituerait une preuve convaincante de sa nature non-Abélienne.

Dans cette thèse, un dispositif à ultra-haute mobilité électronique fabriqué en géométrie Corbino a été adapté pour permettre des mesures du pouvoir thermoélectrique à des températures de quelques millikelvins dans le deuxième niveau de Landau de l'effet Hall quantique fractionnaire. Cette configuration permet de générer des signaux thermoélectriques à basse fréquence grâce à un gradient thermique issu d'une résistance sur puce servant d'élément chauffant localisé. Une méthode développée par d'autres groupes pour la géométrie de barre de Hall a été modifiée et implémentée dans la géométrie Corbino pour calibrer un gradient thermique de façon *in-situ*. En vertu de cette calibration, le pouvoir thermoélectrique longitudinal dans le régime du transport électronique diffusif a été obtenu à partir des signaux thermoélectriques et a été comparé aux prédictions théoriques. Dans cette perspective, aucune observation décisive de l'entropie non-Abélienne n'a été démontrée en raison d'une détérioration inattendue de l'état Hall quantique fractionnaire 5/2 causée par l'ajout de l'élément chauffant résistif micrométrique sur le dispositif. Néanmoins, en s'appuyant sur des comparaisons avec des résultats préalables dans la géométrie Corbino, il est possible de conclure sans ambiguïté que les signaux mesurés sont d'origine thermoélectrique. Ceux-ci constituent une première instance dans la littérature d'une mesure Corbino du pouvoir thermoélectique dans le deuxième niveau de Landau de l'effet Hall quantique fractionnaire.

Acknowledgements

I would first like to thank Prof. Guillaume Gervais for his everyday supervision and dedication to his students, especially in the lab when the dilution refrigerators would not cooperate and his low-temperature expertise and rigor was much needed. For a large portion of this project, I was stuck with no hopes of getting any results, but Prof. Gervais encouraged me to move forward and spent large amounts of time troubleshooting with me until we were eventually successful. This experience and Prof. Gervais' supervision made me improve my technical skills, confidence, and resilience on another level.

Although not directly related to the work presented in this thesis, I was given the opportunity to participate in the bismuth project by assisting Ph.D. student Oulin Yu for two very fruitful experimental campaigns at the National High Magnetic Field Laboratory in Florida. I am grateful to Oulin for letting me contribute to the project even though I was inexperienced in the specifics of thin bismuth devices. I also have to acknowledge again the support of Prof. Gervais who believed in my capacities to undertake this task at the magnet lab, and then later to present a talk about our results at the 30th International Conference on Low Temperature Physics.

I must give a special mention to the support of Ph.D. student Matei Petrescu in the early portions of my project, especially in the previous investigations that he made which laid the foundation of this project and, most importantly, his *world-class* documentation. The statement *standing on the shoulders of giants* could not apply better to what I felt both literally and figuratively when I started my project under his guidance.

My project would not have been possible without the assistance of Sujatha Vijayakrishnan for transferring me all her knowledge of the BlueFors dilution refrigerator, Frédérik Poitevin for thoroughly teaching me the details of the instrumentation and showing me where everything was in the lab, and Talia Martz-Oberlander for showing me how to operate the Oxford 3He refrigerator and answering all my questions regarding various aspects of my experiment. I am also grateful to Zachery Berkson-Korenberg who was extremely helpful in troubleshooting the BlueFors and who spent a handful of Friday evenings with me fixing and preparing the system for yet another cooldown. All of them were also always available to have eye-opening discussions at various stages of my project. Additionally, I wish to thank my colleagues Nick Wicklund, Renée Goodman, Mohammad Abbasi Eskandari, Avram Silberztein, Julien Hacot-Slonosky and Justin Mainville for their assistance in the lab in my first year. The newer members of GervaisLab also deserve a mention, namely, Bodgan Bulgaru for helping me to operate and fix the dilution refrigerator, Edgar Ma for occasionally performing some data acquisition on my behalf, and Didar Sedghi for useful discussions.

I had the chance to get exceptional technical assistance from Richard Talbot, Pascal Bourseguin, and Marc Giroux that were involved in the conception and fabrication of the low temperature sample stage assembly and other parts for the dilution refrigerator system. I would also like to thank Robert Gagnon and John Smeros for their assistance with all the other components needed to run a lab smoothly.

Finally, on another note, I have to acknowledge the state-of-the-art customer support from BlueFors which unconditionally offered their help with spare parts or technical solutions to solve the multiple refrigerator issues that I encountered throughout my Master's degree.

Contributions

The foundational ideas behind this work were envisioned by Prof. Guillaume Gervais as a need to complement a previous experiment which was missing a crucial Corbino thermopower data point to calibrate entropy extracted *via* specific heat. The subsequent design choices for the experimental implementation of the heater to probe thermoelectricity came from a trial and error process with multiple ideas suggested by both Prof. Gervais and me. Then, I adapted the measurement scheme from previous works in the Hall bar geometry and applied it to the specific requirements of the Corbino geometry. I implemented the necessary modifications on the device to generate measurable thermoelectric signals. Additionally, I performed all the data acquisition, experimental manipulation and data analysis presented in this thesis except for the data acquisition of the energy gap after the removal of the heater, which were acquired by Bogdan Bulgaru and Edgar Ma. I operated the dilution refrigerator for the vast majority of the cooldowns where the data presented here was acquired but I was occasionally assisted by Zachary Berkson-Korenberg and Bogdan Bulgaru.

The original design of the low-temperature sample stage assembly was conceived by Frédérik Poitevin and adapted by Richard Talbot, Prof. Gervais and me to satisfy the requirements of the BlueFors dilution refrigeration system. Richard Talbot carried out the computer assisted drawings while Pascal Bourseguin and Marc Giroux machined the parts. The assembly was then installed on the dilution refrigeration unit by Zachary Berkson-Korenberg and me. Finally, the ultra-high mobility Corbino device (CB05) was fabricated by Keyan Bennaceur.

Contents

List of Figures

List of Tables

List of Abbreviations

2DEG two-dimensional electron gas. viii, 2, 3, 4, 5, 6, 7, 17, 29, 36, 37, 40, 42, 44, 48, 57, 58, 67

CF composite fermions. 3, 9, 10, 11, 14

FQH fractional quantum Hall. i, 2, 8, 9, 10, 11, 13, 18, 19, 21, 22, 28, 30, 33, 34, 36, 38, 39, 40, 41, 42, 47, 48, 49, 50, 51, 52, 53, 54, 55, 56, 57, 58, 59

FQHE fractional quantum Hall effect. i, 2, 3, 8, 10, 28, 38, 42, 50, 58

IQH integer quantum Hall. 22, 33, 45, 46, 47

IQHE integer quantum Hall effect. 7, 8, 10, 44, 45, 49

LL Landau level. 7, 19, 20, 44, 45, 58

MBE molecular beam epitaxy. 5, 30

OFHC oxygen-free high-conductivity. 25, 27

QHE quantum Hall effect. 2, 3, 8, 20, 21, 22, 38, 42, 44, 45, 46, 50, 57

RF radio frequency. 29

RIQH reentrant integer quantum Hall. 39, 40, 55

RMS root mean square. 34, 48, 72

SLL second Landau level. i, 2, 11, 15, 22, 39, 40, 41, 49, 50, 54, 55, 58

SNR signal to noise ratio. 73, 75

Chapter 1

Introduction

The exponential growth of computational power from the semiconductor-based transistor industry is now reaching a turning point. Moore's law [1], stating that the number of transistors in an integrated circuit doubles every two years, started saturating about a decade ago. Transistors are now reaching sizes on the order of tens of atoms, consequently pushing the limit of feasibility and demanding a change in computational paradigm. Decades before this issue arose, Feynman was a visionary in 1981 [2], proposing to leverage the mystifying probabilistic properties of quantum mechanics to solve specific problems much more efficiently than with classical computers. Archetypal examples include Shor's algorithm for prime number factorization [3] and simulations of complex quantum mechanical systems such as large molecules.

Recently, there have been extensive research efforts aimed at conceiving a practical quantum computer relying on various physical systems, with the currently most mature being superconducting qubits [4]. Unfortunately, this platform is highly sensitive to environmental perturbations, and the encoded information is lost by decoherence in the matter of hundreds of microseconds. One solution to this problem is to use topologically protected qubits [5]: a theoretically proposed physical system in which the qubits are immune to noise by nature.

Among many others, one promising physical realization of such a system is in the 5/2 state of the fractional quantum Hall effect (FQHE) in the second Landau level (SLL) of extremely clean two-dimensional electron gases (2DEGs). Even though substantial experimental works have improved our understanding of this exotic state, much more compelling evidence is still required to prove that it is non-Abelian and can thus host topological qubits. Based on seminal works on thermopower [6–9], the work presented in this thesis aims to address that question by proposing an experimental scheme to probe non-Abelian entropy *via* longitudinal diffusion thermopower in the Corbino geometry, and presenting preliminary results. This is conveyed throughout this thesis in the following structure.

Chapter 2 builds a comprehensive review of the important physical principles leading to the FQHE while also encompassing the specifics of the Corbino geometry. The 5/2 fractional quantum Hall (FQH) state is then introduced along with experimental works that attempt to shed light on its expected non-Abelian properties. Finally, a review on thermopower is presented, including up to date experimental results and theoretical predictions in the Hall bar and Corbino geometry.

Chapter 3 covers the design details of both the sample stage assembly, which was installed on the dilution refrigerator, and the chip resistor heater which was added on the ultra-high electron mobility Corbino device. The measuring scheme for thermoelectricity is then elaborated on, and some preliminary characterization with the setup is presented.

Chapter 4 discusses several preliminary results obtained with the thermoelectric apparatus described in chapter 3. As such, thermopower transport measurements in the quantum Hall effect (QHE), FQHE, and 5/2 FQH state are compared to previous experimental works or theoretical predictions.

Finally, chapter 5 summarizes the work presented in this thesis and then proposes new avenues for solving technical challenges encountered with the thermoelectric setup. This thesis is also accompanied by several appendices to complement the discussion.

Chapter 2

Background

This chapter concisely introduces the physics of electronic transport in a 2DEG by chronologically covering the QHE, the FQHE, and the composite fermions (CF) picture, leading to a discussion on the $\nu = 5/2$ state and its predicted non-Abelian properties. The emphasis is then oriented toward thermoelectric measurements in different regimes, materials, and geometries in order to establish the theoretical and experimental framework for the focus of this thesis, probing non-Abelian entropy *via* thermopower in the Corbino geometry.

2.1 Two-dimensional electron gas systems

Restricting the motion of electrons to a two-dimensional plane embedded in our three-dimensional world gives rise to the so-called 2DEG. This feat can be achieved in multiple ways, such as an electron trapped at the surface of liquid helium, at a semiconductor-insulator interface (*e.g.* in a metal-oxide-semiconductor field-effect transistor), in a two-dimensional material like graphene, and finally at the interface between two dissimilar semiconductors. While the basic physics required to understand the formation of a 2DEG is similar in these systems, the latter results in the cleanest platform to study many-body electron interactions and is at the origin of the devices used in this thesis.

2.1.1 GaAs/AlGaAs heterostructures

A simplified version of a typical semiconductor heterostructure of GaAs/AlGaAs is shown in Fig. 2.1. The 2DEG, highlighted in blue, arises at the interface between AlGaAs and GaAs from the modulation of the conduction band ϵ_c in the form of a triangular potential quantum well. As a result, the electrons are confined in the lowest energy sub-band provided that the temperature is low enough and the Fermi energy ϵ_F[1] lies beneath the potential barrier. This occurs at temperatures much lower than the separation between the first and zeroth energy sub-bands. Depending on the material, this condition is satisfied anywhere between a few kelvins for GaAs/AlGaAs [10] and room temperature for graphene [11]. As such, electrons within this quantum well will be restricted along the z-axis and behave as two-dimensional particles.

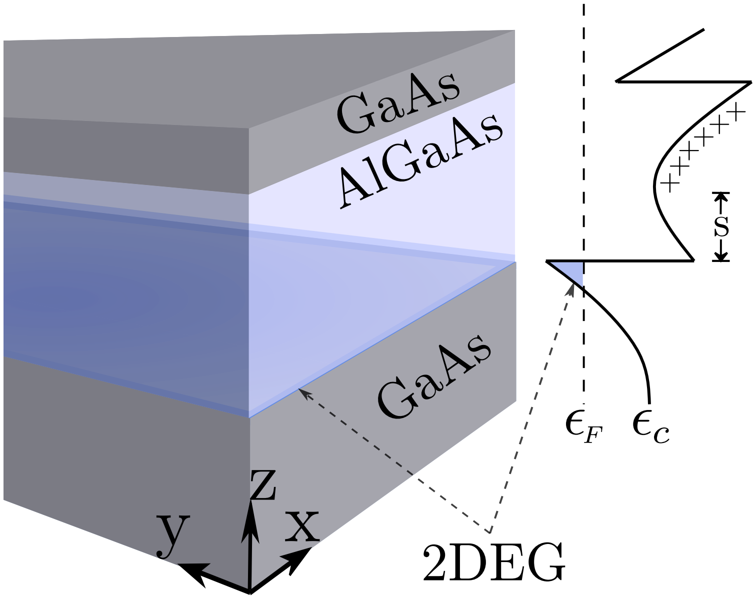

Figure 2.1: Simplified schematic of the layers in a GaAs/AlGaAs heterostructure together with the conduction band of the electrons.

The free electrons are transferred to the 2DEG through n-type doping in the AlGaAs layer using Si:AlGaAs dopants as illustrated by the remaining positive charges. This would

---

[1] The Fermi energy in a 2DEG is given by $\pi\hbar^2 n/m^*$, where n is the electron density and $m^* = 0.067m_e$ is the effective mass in GaAs. Hence, the electron density must be tuned accordingly to position the Fermi energy within the quantum well.

normally impede the transport of electrons and degrade the electron mobility. However, the silicon impurities are introduced at a distance s (called the setback distance) just far enough in the AlGaAs layer to transfer electrons effectively while not disrupting their motion in the 2DEG by scattering. Molecular beam epitaxy (MBE) is the key technology behind the angstrom-precision growth of the layers shown in Fig. 2.1. This process is known as *modulation doping* and recently yielded a world-record ultra-high electron mobility $\mu = 57 \times 10^6$ cm^2/Vs [12]. This translates to an electronic mean free path of roughly 300 μm, which is ideal for observing the many-body physics of highly correlated systems at the foundation of the exotic phenomena observed in this thesis.

2.1.2 Measurement geometries

Typical transport measurements in 2DEG make use of the Hall bar geometry shown in Fig. 2.2b as it gives access to both the Hall and longitudinal resistance. It is well suited for most experiments in 2DEG systems but has one major inconvenience compared to the Corbino geometry sketched in Fig. 2.2a: the unavoidable presence of edge modes in longitudinal transport measurements. This can present an insurmountable barrier to the measurement of exact bulk quantities such as bulk thermal conductance or entropy. Even though a recent study [13] claims to overcome this limitation, the Corbino remains the most effective way to obtain a truly bulk measurement. In that sense, there are important distinctions between the two geometries when dealing with experimentally accessible quantities such as the resistance R and the conductance G. In the Hall bar configuration, one has to carefully reverse the tensor relation in order to relate conductivity σ to resistivity ρ since they become tensors in the presence of a magnetic field as given by

$$\sigma = \begin{pmatrix} \sigma_{xx} & \sigma_{xy} \\ -\sigma_{xy} & \sigma_{yy} \end{pmatrix} = \rho^{-1} = \begin{pmatrix} \rho_{xx} & \rho_{xy} \\ -\rho_{xy} & \rho_{yy} \end{pmatrix}^{-1}, \tag{2.1}$$

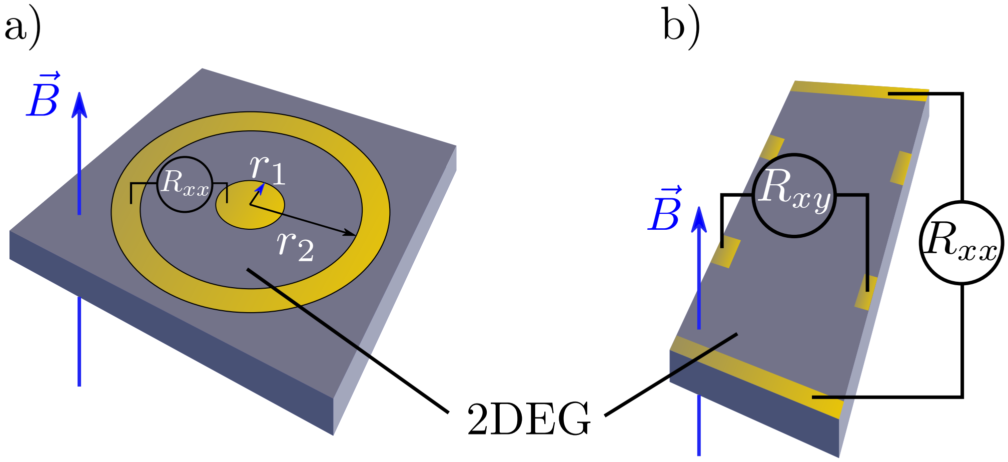

Figure 2.2: a) Schematic of a 2DEG device fabricated in the Corbino geometry showing the measurement of the longitudinal resistance R_{xx}. b) Schematic of the alternative Hall bar geometry where one configuration for probing R_{xy} and R_{xx} is shown.

where ρ_{xy} is defined as the Hall resistivity, which is equal to R_{xy} for a 2DEG. This tensor relation leads to a peculiar result for high magnetic fields[2], where the conductivity is proportional to the resistivity $\sigma_{xx} = \frac{\rho_{xx}}{\rho_{xy}^2}$. In the quantum Hall regime, this relation describes a state with both vanishing resistance and conductance.

Conversely, in the Corbino geometry, the symmetry in ϕ makes the electric field in the ϕ direction E_ϕ equal to zero. Hence, the tensor relation simplifies to a reversible equation $\sigma_{xx} = \rho_{xx}^{-1}$, which is analogous to the behavior of the bulk resistance and conductance relation in a regular three-dimensional material at $B = 0$. However, one still needs to account for the number of squares in a circular geometry given by [14]

$$G = \frac{2\pi\sigma_{xx}}{\ln{(r_2/r_1)}}, \tag{2.2}$$

where r_1 and r_2 are the inner and outer contacts radii respectively as depicted in Fig.2.2a.

---

[2] This happens specifically for $\rho_{xy} \gg \rho_{xx}$. For instance, this condition is satisfied in the quantum Hall plateaus.

2.2 Quantum Hall effects

2.2.1 Integer quantum Hall effect

The integer quantum Hall effect (IQHE) was first observed by Klaus von Klitzing [15] in 1980 and led him to be awarded the Nobel prize in physics in 1985. When a 2DEG system is subjected to a strong perpendicular magnetic field, the electrons move in cyclotron orbits yielding Landau level (LL) quantization of the electronic energy spectrum. To select a given LL, the carrier density n and the magnetic field B are tuned to an integer filling factor given by

$$\nu = \frac{nh}{eB}, \tag{2.3}$$

corresponding to the ratio of the electron density n to the magnetic flux quanta density, *i.e.* $n/(B/\Phi_0)$, where $\Phi_0 = h/e$ is the flux quanta defined by the ratio of Planck's constant h to the elementary charge e. In this scenario, the transport occurs only in the perpendicular direction and yields a quantized transverse Hall resistance R_{xy} and vanishing longitudinal

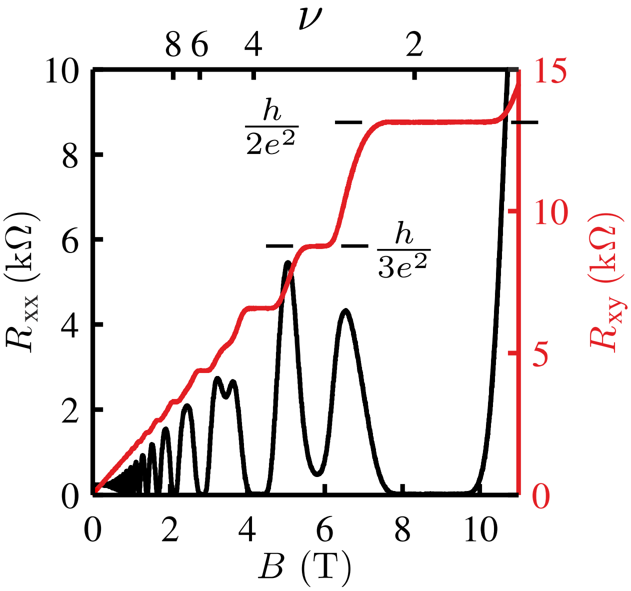

Figure 2.3: Typical IQHE transport measurement, where two visible plateaus at $\nu = 2$ and $\nu = 3$ are indicated. This figure was adapted from Ref. [16].

resistance R_{xx} given by

$$R_{xy} = \frac{h}{\nu e^2}, \qquad R_{xx} \approx 0, \qquad \nu = 1, 2, 3... \; . \tag{2.4}$$

Experimentally, in transport measurements, Hall quantization materializes in the form of finite plateaus in R_{xy} and $R_{xx} = 0$ at the vicinity of integer filling factors as shown in Fig. 2.3. The finite width of the plateaus arises from localized states and is influenced by factors such as the temperature and the amount of disorder in the material [10].

2.2.2 Fractional quantum Hall effect

Shortly after the discovery of the QHE, a significant improvement in the electron mobility μ_e of GaAs/AlGaAs wafers propelled the discovery of the FQHE by Störmer and Tsui in 1982 [17], and they were awarded the 1998 physics Nobel prize for their observation. In the framework of the IQHE, there should be no quantization for non-integer filling factors ν. Yet, Hall plateaus and longitudinal resistance minima were observed at fractional fillings, such as the $\nu = 1/3$ FQH state originally identified by Tsui *et al.* [17] as a consequence of many-body electron-electron interactions in high mobility (low disorder) samples being appreciable enough to favor the creation of a quantized Hall state. Fig. 2.4 represents a typical FQH transport measurement showing the emergence of many fractions. There has been substantial theoretical work aimed at understanding and predicting which fractions should be allowed. The first successful description is attributed to Robert B. Laughlin [19] who was awarded the 1998 Nobel prize in physics. In his work, he proposed a wavefunction that accurately described the observations associated with the 1/3 state and by extension other FQH states of the form $1/q, \quad q = 1, 2, 3...$. Subsequently, Haldane proposed a hierarchical model [20] based on a continued fraction starting with a known parent state to explain the sequence of *odd* denominator states which were experimentally observed at the time. However, this model fails to capture the complete plethora of fractional states occurring at *odd* denominator

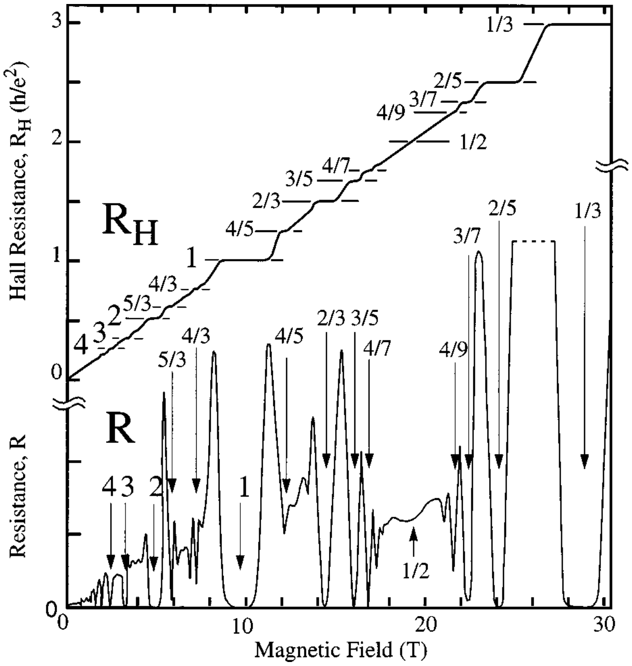

Figure 2.4: Magnetotransport of a GaAs/AlGaAs sample showing a multitude of well-developed FQH states. Figure reproduced from ref. [18].

states, requiring the need for a more elaborate model.

2.2.3 Composite fermions picture

Here, the composite fermions (CF) model devised by Jainendra K. Jain [21] offers the most complete and comprehensive explanation for *odd* denominator states. The paradigm proposed in this model is to think in terms of composite particles generated by flux quanta attached to electrons. For instance, as illustrated in Fig. 2.5a, the $\nu = 1/3$ state can be understood as electrons pairing with three flux quanta. The resulting wavefunction is symmetric (bosonic) since it combines the wavefunction of an electron (antisymmetric) to the wavefunctions of three flux quanta (antisymmetric). This yields a favorable condition for the collective composite particles to condense into a quantum Hall state.

Conversely, as represented in Fig. 2.5b, at filling factor $\nu = 1/2$, the pairing occurs between an electron and two flux quanta, generating an anti-symmetric (fermionic) wavefunction. The $\nu = 1/2$ composite particles [22] behave drastically differently than the bosonic

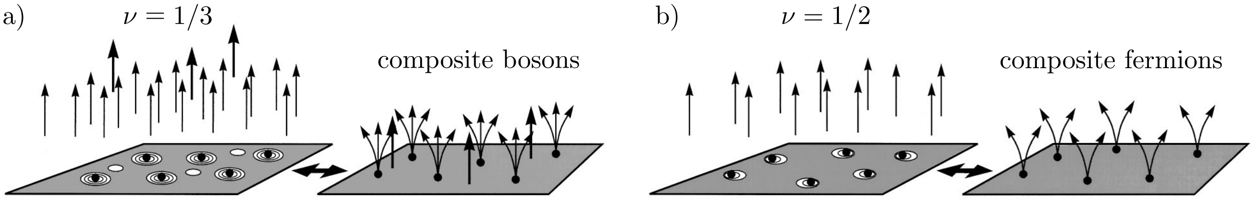

Figure 2.5: Illustration of the flux quanta pairing with electrons for filling factors of $\nu = 1/3$ in a) and $\nu = 1/2$ in b). Figure adapted from Ref. [18].

composite particles at $\nu = 1/3$ since they exhibit fermionic statistics and thus act as a Fermi liquid [23]. Then, the CFs, pairing $2p$ flux quanta with one electron, now experience a reduced effective magnetic field of $B^* = B - 2pn\Phi_0$, which is identically zero at exact filling factor $\nu = 1/2$. As such, the FQHE can be understood as the IQHE of CFs where B^* replaces the external magnetic field B and free electrons are replaced by free CFs. In this picture, Hall quantization occurs for

$$\nu = \frac{p}{2p \pm 1}, \quad p = 1, 2, 3, \ldots \, , \tag{2.5}$$

which then explains the experimentally identified *odd* denominator FQH states.

2.2.4 The elusive $\nu = 5/2$ state

The universality of the CF model for predicting fractional quantum Hall states fails for some *even* denominator states. One archetypal instance is the $\nu = 5/2$ state discovered by R. Willett [24] in 1987 which remains to this day not fully understood, *i.e.* there is still a persistent debate on the exact structure of its wavefunction. As such, many-body wavefunctions based on Pfaffian states [25, 26], anti-Pfaffian states [27, 28], and more recently their particle-hole symmetric form [29] have been theoretically proposed with different degrees of agreement with experimental and numerical works (see Ref. [30] for a complete review of the $\nu = 5/2$ state).

This state is in principle prohibited by the CF picture, yet it experimentally shows as a proper FQH gaped state with a Hall plateau at $R_{xy} = \frac{eh}{n(5/2)}$ and a $R_{xx} \to 0$ minimum. In a simplistic manner, its existence can be rationalized by considering the enhanced electron-electron interactions in the SLL which lead to a paired state and a Pfaffian wavefunction that is analogous to a $p_x + ip_y$ superconductor in BCS theory [5]. As a result, the conditions to experimentally manifest it in GaAs/AlGaAs are stringent. Notably, temperatures below 100 mK and electron mobility exceeding 1×10^6 cm^2/Vs are necessary conditions since its energy gap is reported to be at most $\sim$ 450 mK [31], even though graphene systems now offer much more accessible energy gaps for *even* denominator states in the range of a few Kelvins [32].

2.2.5 Non-Abelian anyons and topological quantum computations

The theoretical descriptions for the $\nu = 5/2$ FQH stand out for predicting that the $\nu = 5/2$ could host non-Abelian anyonic quasiparticles with an effective charge of $e^* = e/4$, which could be a possible platform for the implementation ot topologically protected qubits. Abelian anyons in their abstract form were first theoretically envisioned by Frank Wilczek in 1982 [33]. Their existence is a consequence of two-dimensions, and they can be described as a two-particle wavefunction that gains an arbitrary phase factor $e^{i\phi}$ upon exchange, as depicted in Fig. 2.6a. This contrasts sharply with conventional three-dimensional particles in which there are only two outcomes, *i.e.* ±1 for bosons or fermions. Renowned theoretical physicist B. I. Halperin later reconciled this idea with the composite particles in FQH states and related the exchange phase to their fractional statistics [34]. Regular FQH *odd* denominator states described by the CF model behave as anyonic quasiparticles with fractional statistics. Conversely, it is not generally agreed upon as to what class of statistics the $\nu = 5/2$ state belongs, but theoretical evidence, such as the Moore-Read description [25], and numerical works [36] point toward non-Abelian statistics. A non-Abelian ensemble is a braiding group in which braiding operators do not commute with one another. For example, a braiding group consisting of three particles will possess two braiding operators σ_1 and σ_2, as shown

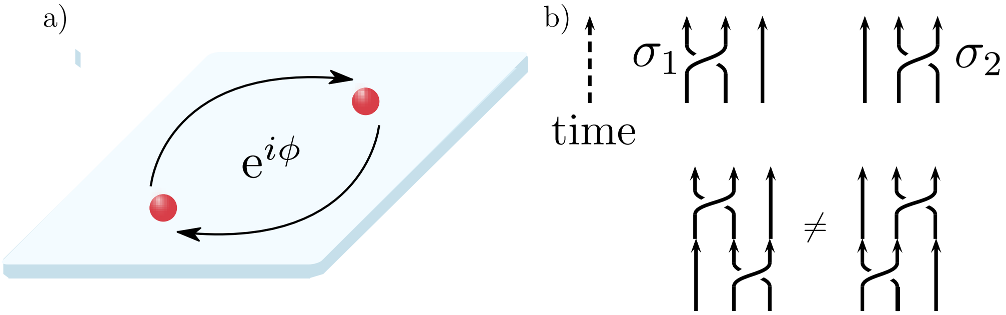

Figure 2.6: a) Two anyons gaining a phase of $e^{i\phi}$ in their wavefunction upon exchange. Figure adapted from ref. [35]. b) Non-commuting braiding operation for non-Abelian anyons. Figure adapted from ref. [5].

schematically in Fig. 2.6b. These particles are designated as non-Abelian if the resulting wavefunction of first applying σ_1 followed by σ_2 is different than first applying σ_2 followed by σ_1, as described mathematically by the relation

$$[\rho(\sigma_1)]_{\alpha\beta}[\rho(\sigma_2)]_{\beta\gamma} \neq [\rho(\sigma_2)]_{\alpha\beta}[\rho(\sigma_1)]_{\beta\gamma}, \tag{2.6}$$

where $[\rho(\sigma_1)]_{\alpha\beta}$ is a unitary matrix acting on the wavefunction ψ_β of the three particles state that implements the braiding operation $\psi_\alpha \rightarrow [\rho(\sigma_1)]_{\alpha\beta}\psi_\beta$.

Another hallmark of the Moore-Read description is the highly degenerate Hilbert space in which the quasiparticles evolve into. This property that allows braiding statistics is key for the implementation of topological quantum computations since it allows one to instantiate qubits and apply quantum gates using braiding operations in this degenerate Hilbert space. Otherwise, in the case of Abelian anyons, the braiding operations generate trivial transformations of the ground state. Furthermore, the inherent fault protection obtained using non-Abelian anyons originates from the following properties: i) the braiding itself is independent of the exact path taken by the quasiparticles; ii) the set of degenerate states is protected by an energy gap[3]; and (iii) the quasiparticles can only interact with themselves, *i.e.* they are immune to electron-phonon interactions and the hyperfine electron-nuclear

---

[3] As long as the system is kept at a sufficiently low temperature and low frequency excitations compared to the energy gap, the quasiparticles will not experience decoherence.

interaction [5].

2.2.6 Experiments probing non-Abelian anyons entropy

There is however a major caveat to the previous discussion about fault-tolerant quantum computations: there is not yet an irrefutable experimental proof that non-Abelian anyons materialize in real physical systems such as the $\nu = 5/2$ FQH state. Nevertheless, there is suggestive evidence by various works in GaAs and graphene systems that support their existence. Notably, Fabry-Perot electron interferometry [37–43], quasiparticle charge measurement *via* shot noise [44], and thermal Hall conductivity [45–51] are all pointing towards the underlying non-Abelian nature of the $\nu = 5/2$ FQH state to have a wavefunction with a topological order hosting non-Abelian quasiparticles. As will be discussed below, another promising approach is to probe the entropy at low temperatures to gain insights on the structure of the ground state .

Non-Abelian entropy

One can in principle leverage the highly degenerate ground state of non-Abelian anyons by probing the excess dimensional entropy. According to the Moore-Read description of the 5/2 state, the degeneracy of the ground state for N_q quasiparticles is given by d^{N_q}, where $d = \sqrt{2}$ is the quantum dimension[4] of this class of quasiparticles. As a result, the dimensional entropy $\mathcal{S}_d$ for non-Abelian anyons is given by [6, 52]

$$\mathcal{S}_d = N_q k_B \ln d, \tag{2.7}$$

where k_B is Boltzmann's constant. While this approach removes the need to fabricate elaborate Farby-Perot interferometer patterns on the sensitive wafers, it however contains another

---

[4] The quantum dimension corresponds to the asymptotic degeneracy per particle in the generate Hilbert space of the ground state. For Abelian quasiparticles, d = 1 and $d > 1$ for non-Abelian quasiparticles. For instance, for the Moore-Read state, $d = \sqrt{2}$, but $d = (1 + \sqrt{5})/2$ in the case of Fibonacci anyons [5].

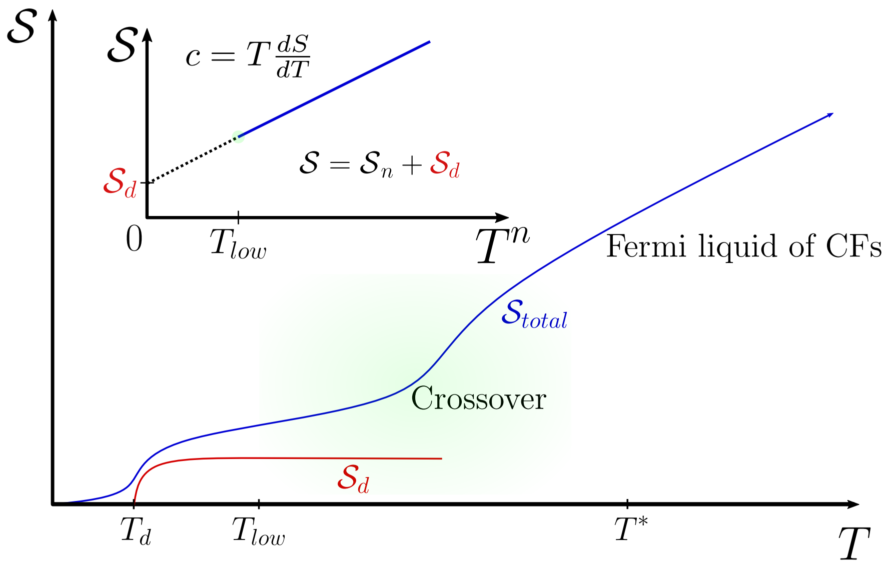

Figure 2.7: Entropy as a function of temperature showing the ideal regime to probe non-Abelian properties. The inset shows how to extract the entropy from the specific heat. Figure adapted with permission from Ref. [14].

set of difficulties. The temperature range in which the entropy S_d is experimentally accessed must be carefully selected, as detailed in Fig. 2.7. If the temperature is greater than T^*, the entropy would be dominated by phonon contributions[5], Fermi liquid CFs, or positional entropy. On the other hand, if the temperature is colder than the degeneracy temperature T_d, the coupling between quasiparticles becomes non-negligible and is unavoidably lifting the degeneracy of the ground state. Therefore, the ideal temperature range should be between these two regimes, as shown in Fig. 2.7 by T_{low}[6], where ideally the experiment should be performed in its vicinity.

Specific heat

One approach to extract non-Abelian entropy is to infer it by integrating the temperature dependence of the specific heat with respect to temperature. Specific heat is defined in terms of entropy by the thermodynamic relation $c = T\frac{dS}{dT}$, implying that the entropy can be

---

[5] Phonons are expected to become negligible in the thermopower signal below ~ 200 mK in GaAs [7].

[6] According to numerical estimations in GaAs systems, T_{low} should roughly be between $T_d \approx 7$ mK and $T^* \approx 300$ mK [6].

accessed by

$$\mathcal{S}(T) = \mathcal{S}_0 + \int_{T_{low}}^{T} \frac{c}{T'} dT', \tag{2.8}$$

where $\mathcal{S}_0$ is an offset from the integration that has to be determined by other means. The dimensional entropy $\mathcal{S}_d$ can then be extracted by fitting the resulting $\mathcal{S}(T)$ curve to deduce the zero-temperature limit and thus estimate $\mathcal{S}_d$, as shown in the inset of Fig. 2.7.

This scheme was implemented in the Gervais group in a high-mobility Corbino device [14, 53–55] by using the simple relation $C = K\tau$ to extract the heat capacity C and convert it to specific heat c. However, the main issue for obtaining an exact absolute value for the entropy from this technique is the $\mathcal{S}_0$ integration constant in eq. (2.8), which was estimated and reported in Ref. [54] by the Gervais group using previously established longitudinal thermopower S_{xx} data from Ref. [9]. Even though the temperature dependence of c closely matches S_{xx}, the data from Ref. [9] originates from a different device having similar density and mobility, and a completely different geometry, *i.e* a Hall bar. Hence, it is questionable whether the entropy calculated in this way was physical and could adequately be compared to the Yang and Halperin theory based on a Pfaffian state.

This conclusion leads to the main objective of this thesis, *i.e.* to measure the longitudinal thermopower in the eaxct same Corbino device that was used to measure the specific heat [55]. In doing so, it would provide a definitive estimate for $\mathcal{S}_0$ as well as new thermopower data absent from the literature for the Corbino geometry in the SLL. Towards this goal, in the next section, we will introduce the necessary background and the relevant literature required to understand thermopower experimental concepts and their relation to non-Abelian entropy.

2.3 Thermopower

2.3.1 The Seebeck effect

In 1822, Thomas J. Seebeck discovered that two dissimilar metallic junctions held at different temperatures would deflect a magnet. This experiment was later understood as the result of a potential ΔV induced by a thermal gradient ΔT which generates a current around a closed loop circuit, hence deflecting the magnet by Ampère's law. The strength at which a material can produce a thermovoltage is given by the Seebeck coefficient, or thermopower, defined as

$$S = -\frac{\Delta V}{\Delta T}. \tag{2.9}$$

The mechanism for thermopower is attributed to an equilibration of charges that were displaced by the thermal current originating from a thermal gradient. This leads to a measurable voltage with an opposite sign relative to ΔT as illustrated in Fig. 2.8.

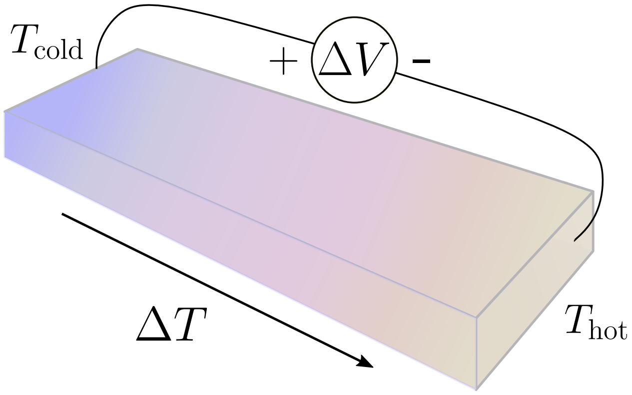

Figure 2.8: Generic illustration of the Seebeck effect in a three-dimensional material in the absence of a magnetic field.

For metals, the Seebeck coefficient is typically on the order of a few μV/K whereas it can be on the order of a few hundreds of μV/K for semi-conductors [56]. To observe thermoelectricity, the electric current density $\mathbf{J_e}$ in the device must be identically zero. This can be understood using Boltzmann's equations for thermal and electronic transport in the absence of a magnetic field [57]. As such, these equations can be expressed in a compact matrix form as

$$\begin{pmatrix} \mathbf{J_e} \\ \mathbf{J_Q} \end{pmatrix} = \begin{pmatrix} \sigma & \sigma S \\ \sigma \Pi & \kappa \end{pmatrix} \begin{pmatrix} -\nabla V \\ -\nabla T \end{pmatrix}, \tag{2.10}$$

where $\mathbf{J_Q}$ is the heat current density, Π is Peltier's coefficient, κ is the thermal conductivity, and σ is the electrical conductivity. When the electric current is set to zero, *i.e.* $\mathbf{J_e} = 0$, the first row of the matrix equation yields $S = -\frac{\nabla V}{\nabla T}$. The addition of a magnetic field or an anisotropy in the material complicates the problem and the elements in the matrix become tensors. In particular, the thermopower separates into the longitudinal thermopower S_{xx}, and the Nerst (transverse) coefficient S_{xy}. The thermal transport leading to a measurable thermopower can be dominated by phonons (phonon-drag) or electrons (diffusion thermopower) depending on experimental conditions such as the temperature at which the experiment is performed. Note that the latter is the relevant thermopower regime to probe the transport of quasiparticles, and in this work, the focus will only be on the longitudinal diffusion thermopower S_{xx} since in a Corbino geometry, $S_{xy} \equiv 0$.

2.3.2 Longitudinal thermopower and entropy in clean 2DEGs

As briefly mentioned in the previous section, there is a direct relation between entropy and longitudinal diffusion thermopower of a 2DEG. Albeit, that relation deeply depends on the measurement geometry used experimentally.

Hall bar geometry

In a Hall bar device, in the clean limit[7], the longitudinal thermopower S_{xx} is related to the *entropy per electron per electron charge* [6]

$$S_{xx} = -\frac{\mathcal{S}}{|e|N_e}, \tag{2.11}$$

---

[7] The clean limit is achieved for $\omega_c \tau_m \to \infty$, where ω_c is the cyclotron frequency and τ_m is the momentum lifetime. For our ultra-high mobility sample, this is obtained for fields of a few mT. A rigorous definition of this limit is discussed in detail in Ref. [58].

where N_e is the number of electrons contributing to the transport. The number of excited quasiparticles near the center of a quantum Hall plateau is given by [6]

$$N_q = \left| \frac{e}{e^*} \frac{B - B_0}{B_0} \right| N_e, \tag{2.12}$$

where e is the charge of the electrons, e^* is the effective charge of the quasiparticles[8], and B_0 is the field at the center of the quantum Hall plateau. In the above expression, $\left|\frac{e}{e^*} N_e\right|$ corresponds to the number of N_q quasiparticles created for a given number of electrons N_e, and $\left|\frac{B-B_0}{B_0}\right|$ is the fraction of excited quasiparticles arising from a deviation from the center of the quantum Hall plateau. Thus the product of these two expression yields the number of excited quasiparticles or quasiholes as expressed by eq. (2.12). Combining eqs. (2.7), (2.11), and (2.12) results in an experimentally accessible expression that allows to extract the quantum dimension d, assuming a known value for e^*, *i.e.*

$$S_{xx} = - \left| \frac{k_B}{e^*} \frac{B - B_0}{B_0} \right| \ln d. \tag{2.13}$$

The Hall bar longitudinal thermopower is therefore proportional to the absolute value of B and remains negative across the FQH plateau.

Corbino geometry

In the case of a Corbino disk, also in the clean limit, Barlas and Yang found a drastically different behavior, where the longitudinal thermopower is related to the *entropy per quasiparticle per quasiparticle charge* [8]

$$S_{xx} = \frac{\mathcal{S}}{e^* N_q}. \tag{2.14}$$

---

[8] The theoretical descriptions of non-Abelian quasiparticles support an effective charge $e/4$ for the 5/2 FQH state. However, quasiparticles with an effective charge of $e/2$ have also been measured in shot noise measurements at $\nu = 5/2$ [59].

Substituting $\mathcal{S}$ by the dimensional entropy defined in eq. (2.7) yields the following expression for the longitudinal Corbino thermopower

$$S_{xx} = \frac{k_B}{e^*} \ln d. \tag{2.15}$$

As a result, in the Corbino geometry the sign of S_{xx} is expected to change when the transport switches from quasiparticle to quasihole dominated and the sign of e^* changes. However, the magnitude of S_{xx} remains finite and constant in the FQH plateau. This contrasts with the Hall bar longitudinal thermopower where the magnitude of S_{xx} follows $|B|$ in the vicinity of B_0.

2.3.3 Longitudinal thermopower in the quantum Hall effect

Characteristic features of the longitudinal diffusion thermopower in the Hall bar geometry include $-S_{xx}$ vanishing at the center of LLs and taking positive values between LLs, and the magnitude of the peaks associated with the LLs increasing with magnetic field and temperature. As shown in Fig. 2.9a, this behavior is predicted by theory [60, 61] and was observed experimentally [62, 63]. Again, from the fundamental distinction between Hall bar and Corbino thermopower illustrated by eqs. (2.11) and (2.14), their behavior contrasts

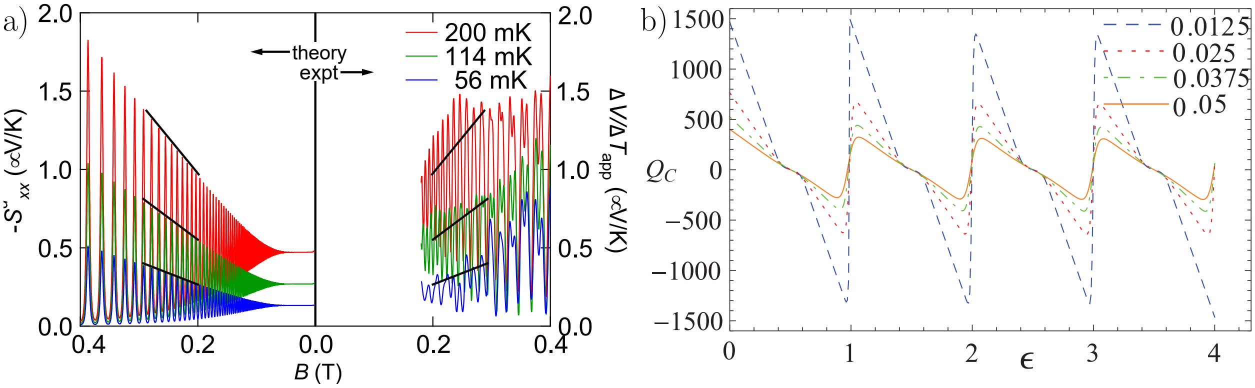

Figure 2.9: a) Measured Hall bar thermopower compared to simulations in the QHE reproduced from Ref. [62]. b) Simulated Corbino thermopower in the quantum Hall effect reproduced from Ref. [8].

sharply. As shown in Fig. 2.9b, Corbino thermopower changes sign at the center and between LLs since the transport shifts from particle dominated to hole dominated, a behavior reminiscent of the *entropy per quasiparticle per quasiparticle charge* description predicted by Barlas and Yang [8]. Furthermore, close to the center of the LL, the magnitude of S_{xx} is expected to increase as a function of decreasing temperature [64].

Multiple groups [65–67] have attempted to study the Corbino thermopower in the quantum Hall regime with varying degrees of agreement with the theory. These studies differ in the way that the thermal gradient was induced in the device. As such, the first study [65] generated a thermal gradient by making use of a laser spot focusing on the center contact of the Corbino device as depicted in the inset of Fig. 2.10a. The authors labeled the recorded signal as *photovoltage* since it is *a priori* induced by light even though they claim to have measured thermovoltage. This signal captures some expected features of the Corbino thermopower except for the sign reversal at LLs. The same problem subsists in a subsequent study [66] where the thermopower signal does not convincingly display a symmetric sign reversal. In the latter, the thermal gradient was created with microwave radiation in a concentric waveguide on the outer contact of the device. More recently, in a study by Real *et al.* [67], more conclusive results were obtained using an on-chip resistive heater patterned within the inner contact of the device as shown in Fig. 2.10c. This design allows one to employ the standard quasi-DC lock-in technique and obtain more precise results[9]. The thermovoltage V_{tp}, shown in Fig. 2.10c, captures the symmetric sign reversal at the correct locations. The large spurious signals appearing at exact filling factors are an unexplained artifact of imposing a thermal gradient in insulating QHE states. A common problem with these works is the lack of a defined temperature gradient across the device contacts, although Real *et al.* recently made progress in that direction [68, 69]. This hinders a precise quantitative assessment between results from different devices and additionally makes it difficult to

---

[9] Purely DC measurements typically suffer a background from residual thermoelectric voltages at the devices contacts.

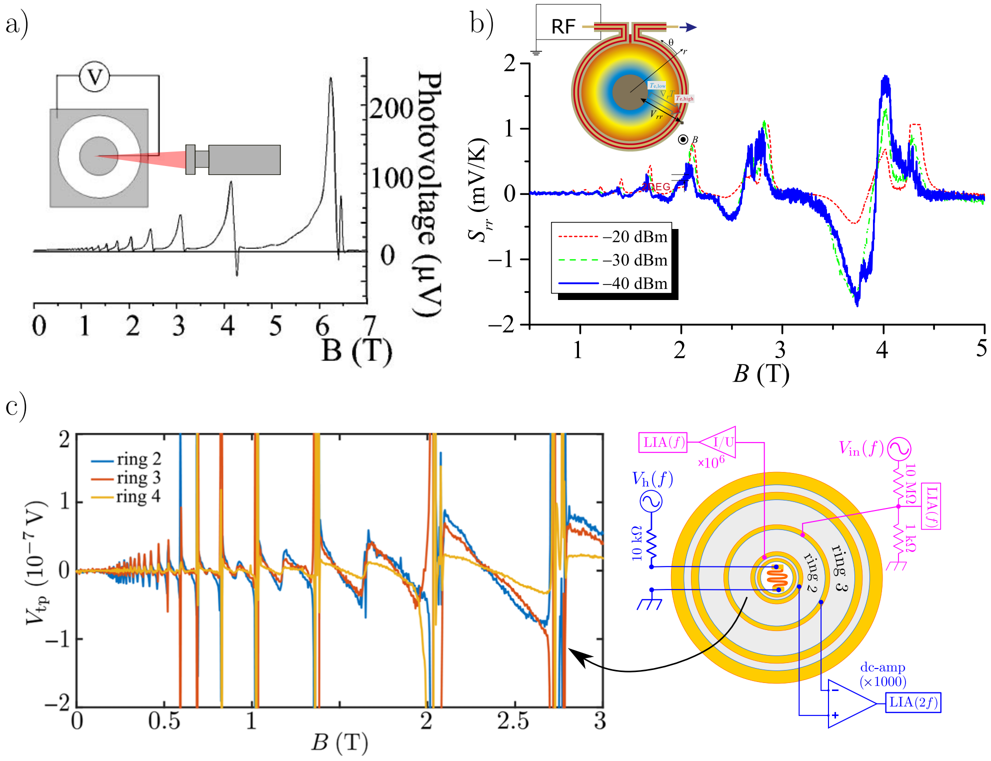

Figure 2.10: Corbino thermopower results in the QHE adapted and reproduced from a) Ref. [65], b) Ref. [66], and c) Ref. [67].

measure the temperature dependence of the Corbino thermopower. From Ref. [67]'s results, there is suggestive evidence in Fig. 6 for $S_{xx}(T)$ to decrease with increasing temperature as proposed theoretically [64]. The caveat is that the heating power is kept constant as the temperature is increased which would result in a reduced ΔT, consequently reducing ΔV with temperature. Hence, the data from this experiment remains inconclusive.

2.3.4 Longitudinal thermopower in the fractional quantum Hall effect

Longitudinal diffusion thermopower data for the Corbino geometry in the FQH regime is absent from the literature but is well-established in the case of the Hall bar geometry. Fig. 2.11 presents a selection of recent results by different groups [9, 70], for a variety of FQH states. The general qualitative behavior of $-S_{xx}$ in the FQH regime is similar to the

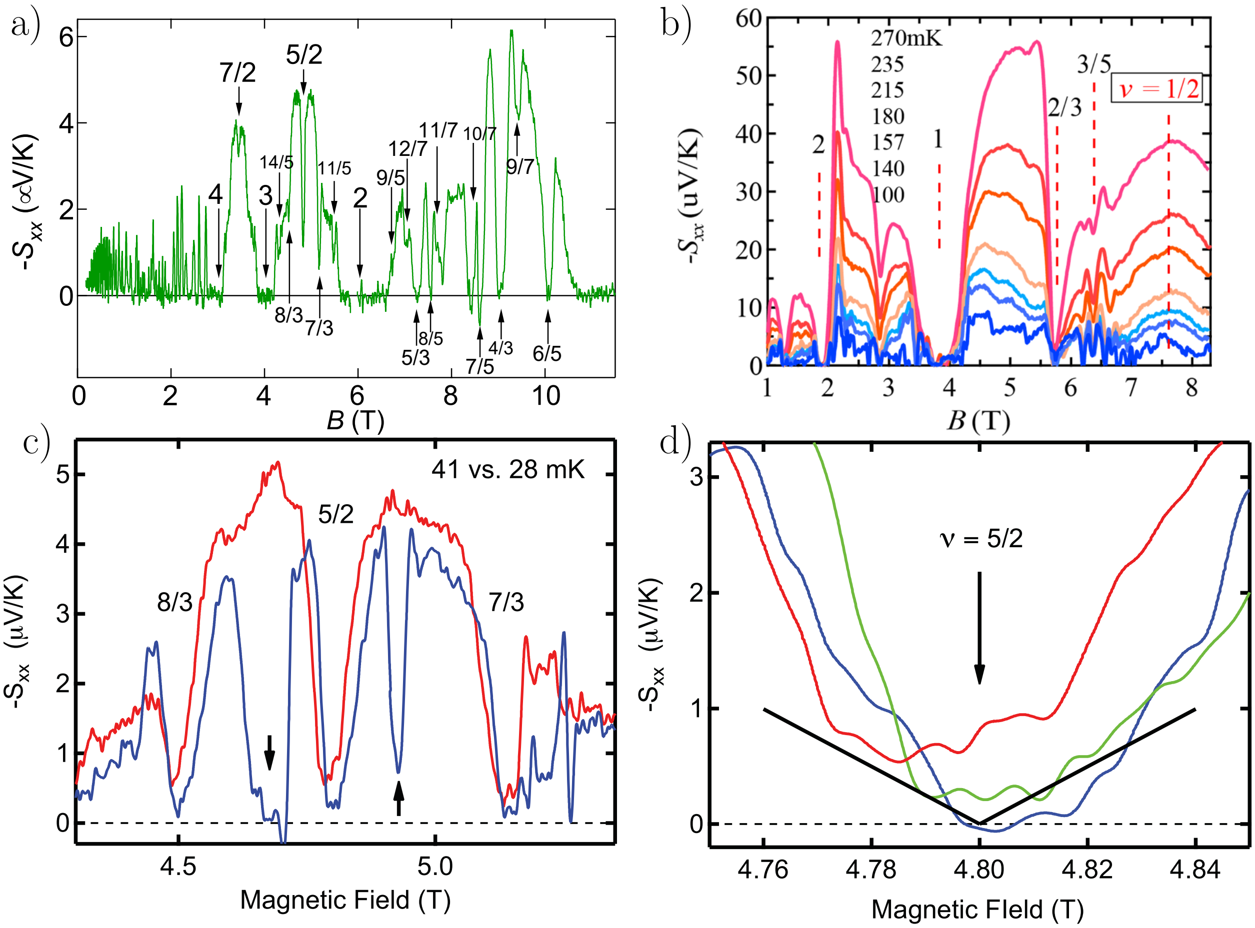

Figure 2.11: a) Figure reproduced from the Caltech group, Ref. [62], showing a multitude of FQH states detectable with thermopower in a device with a similar density than the Corbino device used in our work. b) Thermopower data from Ref. [70] in a device with a lower density, featuring the temperature dependence of IQH and FQH states. c) Figure reproduced from Ref. [9] for the same device as in a) in the SLL. d) Hall bar thermopower in the vicinity of the $\nu = 5/2$ FQH state from Ref. [9].

QHE regime in the sense that a vanishing $-S_{xx}$ coincides with a FQH state and the signal increases with increasing temperature as seen in Figs. 2.11a,b,c. Additionally, focusing on the 5/2 FQH state, an appreciable attempt to experimentally reproduce the behavior of eq. (2.11) was made by Chickering *et al.* [9] and reproduced here in Fig. 2.11d. This result shows hints of the expected non-Abelian trend as the temperature is lowered to 20 mK but remains non-compelling evidence for a non-Abelian entropy given by the highly-degenerate Hilbert space. There was also an attempt in a Hall bar bilayer graphene device in which there exists a richer set of *even* denominator states to explore compared to GaAs systems. The data

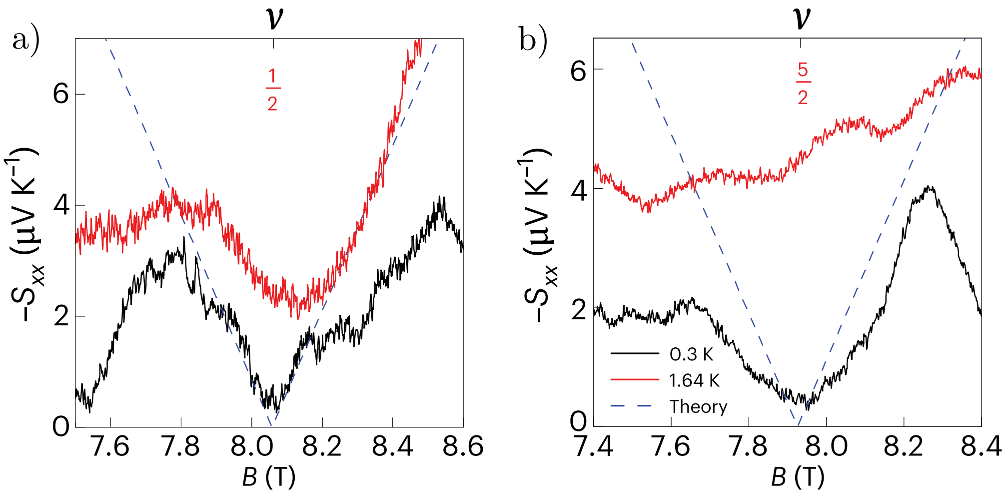

Figure 2.12: Figure reproduced from ref. [63]. Thermopower in a bilayer graphene device along with its associated theoretical prediction for a) the $\nu = 1/2$ state and b) the $\nu = 5/2$ state.

from Ref. [63] at low temperature (300 mK) shown in Fig. 2.12 shows weak evidence for the presence of non-Abelian entropy. These preliminary results justify the need to search for more definitive evidence, and as suggested by the authors of Ref. [9], the Corbino geometry could potentially provide a more quantitative approach to probing non-Abelian entropy, hence the focus of this work.

Chapter 3

Methodology

This chapter covers the experimental details pertaining to the devices, instruments and measurements involved in probing Corbino thermopower. First, the design of the sample stage assembly attached to the dilution refrigerator is reported. Secondly, the design constraints and details of the thermovoltage setup are described. Finally, the details of the thermovoltage circuit are explained along with the scheme required to generate a known temperature gradient.

3.1 Design of a sample stage assembly for a dilution refrigerator

All the low-temperature and magnetic field data presented in this thesis were acquired in a BlueFors LD250 dilution refrigerator unit equipped with a 9 T superconducting magnet. For enhanced thermal efficiency between the samples and the dilution refrigeration unit, the devices are wired from the mixing chamber[1] to room temperature *via* thermocoax cables. These cables have an appreciably high linear resistance of about $\sim 50\ \Omega/\text{m}$, making them

---

[1] The mixing chamber is the final stage of a dilution unit, where a base temperature below 7 mK is routinely achieved in our system.

the optimal trade-off between a good electrical conductor and a bad thermal conductor[2]. From the mixing chamber to the sample stage, maximum thermal contact is required for the device contacts to be as cold as possible. Hence, this justifies the choice of routing oxygen-free high-conductivity (OFHC) copper coaxial cables down to the device stage. Moreover, the use of coaxial cables minimizes the excess noise or heat leaks coming from unwanted sources of electromagnetic or thermal radiation. For the same reason, the device is also encapsulated in a copper Faraday cage (see Fig. A.1 in appendix A).

The sample stage is a crucial component of a functional low-temperature high magnetic field apparatus. The sample stage is positioned at the center of the magnetic field center and is thermally connected to the mixing chamber in order to cool the devices down to below $\sim$ 10 mK. This setup was designed *in-house* since dilution unit users have many different needs and constraints. Here, a new sample stage was designed to overcome a temperature limitation arising from excess vibrations reaching the system. The design constraints and the material choices required to achieve the best sample stage base temperature are stringent and intertwined, mainly because of the low-temperature (below 7 mK) and high magnetic field (up to 9 T) of the system. The main constraints are listed as the following: i) restricting to the use of non-magnetic materials and minimizing eddy currents; ii) high thermal conduction and low heat capacity between the mixing chamber and the sample stage; iii) strong mechanical rigidity; iv) must fit with at least 5 mm of clearance within the magnet bore; v) must allow enough space to accept four devices and the associated wiring.

To satisfy constraints i), ii), and v), a design intended for a different dilution system (Oxford Triton [71]) was adapted for the BlueFors dilution unit. This mostly concerns the choice of materials and the geometry of the bottom plate where the samples are installed.

Fig. 3.1 offers a detailed schematic of the sample stage assembly regarding the geometry and the choice of materials. OFHC copper was chosen as the top plate and support rings

---

[2] Otherwise the cables would conduct heat from room temperature to mK temperatures and be a major source of heat leak, *i.e.* warming up the mixing chamber stage.

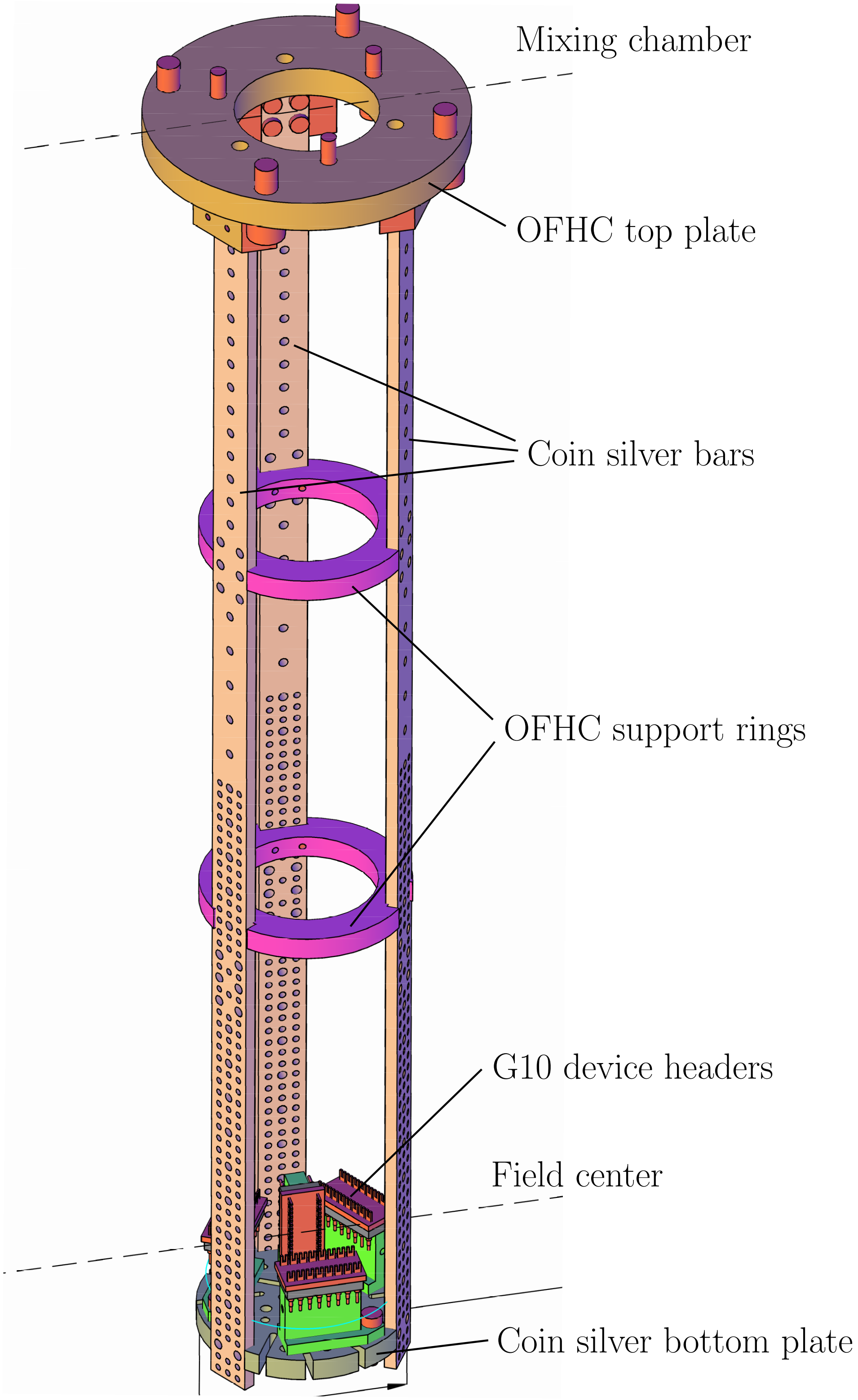

Figure 3.1: Schematic of the sample holder assembly designed to cool samples below 10 mK in the 3 inch bore of a superconducting 9 T magnet.

that connect to the mixing chamber stage for its superior thermal conductivity and low heat capacity. Coin silver was chosen for the support bars and bottom plate since it offers the best trade-off between thermal conductivity and mechanical rigidity. An array of holes was drilled in the support bars in the region where the magnetic field is strong[3] to mitigate the effect of eddy current heating by cutting the current loops generated by a time varying magnetic field. The same principle was applied to the bottom plate and support rings where overlapping slits were cut in the plate. The heat leak from eddy currents is given by [72]

$$\dot{Q}_e = \frac{r^2 V \dot{B}^2}{8\rho}, \tag{3.1}$$

for a filled disk of radius r, volume V, and resistivity ρ. Assuming the OFHC copper bottom plate to be filled, $\dot{Q}_e$ is estimated to be ~ 22 μW for a magnetic field sweep rate of $\dot{B} = 50$ mT/min. This is significantly higher than the ~ 13 μW cooling power at 20 mK of the BlueFors dilution unit and will inevitably lead to an increase in base temperature. Hence, mitigating $\dot{Q}_e$ by cutting the current paths with slits and holes is crucial. Moreover, a fast thermal response time to cool back down to base temperature efficiently following a magnetic field sweep is also important. For quantitative estimates of the thermal response time, *i.e.* the figure of merit for the thermalization of the assembly to the mixing chamber, see Ref. [71]. These values slightly underestimate the response time of the BlueFors sample stage assembly since they apply to a shorter design. Finally all the parts of the assembly were electrochemically gold-plated with a thickness of ~ 800 nm to protect them from oxidation, increase the surface reflectivity[4], and enhance the thermal contact between parts.

In order to satisfy constraints iii) and iv), the pre-existing 28 cm long design from Ref. [71] was adapted for a 38 cm long sample stage. Since the BlueFors sample stage had to be made 10 cm longer, two support rings were added to reinforce the structure of the apparatus.

---

[3] The magnetic field drops by 90 % at $z = 13$ cm away from the field center. Therefore, the support ring was installed, and the holes were drilled until approximately that distance to reduce eddy currents.

[4] A more reflective surface will emit and absorb less black-body thermal radiation.

The enhanced structural strength was also required to reduce mechanical vibrations in the sample stage since it becomes a huge source of eddy current heat leak in a strong magnetic field [72]. For the same reason, two ruthenium oxide (RX-102B-CB) thermometers were installed below the bottom plate to ensure that a reasonable base temperature was obtained at the sample stage. They were calibrated in previous cool-down runs at the mixing chamber stage down to 7 mK since achieving a base temperature below 20 mK is crucial to obtain a near perfectly collapsed 5/2 FQH state.

For a lengthy portion of this work, a large mechanical vibration was propagating to the sample stage and led to a sub-optimal base temperature of above 100 mK in a magnetic field. This was caused by an incorrectly installed attenuation plate holding a scroll pump in the gas handling system of the cryostat. As a result, this was hindering the formation of the 5/2 FQH state. This problem was partially solved with the new mechanically rigid sample stage assembly and then fully resolved by eliminating the vibration at the source.

3.2 Thermoelectric experiment in an ultra-high electron mobility Corbino device

3.2.1 Design considerations

Having now met the experimental requirements to measure thermopower in the FQHE regime with the sub-10 mK sample stage in a 9 T magnetic field, the conception of a setup for measuring thermopower can be considered. Historically, typical thermopower experiments consist of two thermometers and two voltage probes at both ends of a sample with one side held at base temperature *via* a thermal ground while the other side is heated [56,57]. In spite of the simplicity of this approach, it is difficult to implement in micrometer-scale samples of ultra-high mobility ($> 20 \times 10^6$ cm^2/Vs) since directly patterning thermometers or heaters on the wafer significantly degrade its electronic mobility. To mitigate this, we opted to use the device itself as an *in-situ* thermometer, a technique implemented successfully in the past by other groups working with ultra-high mobility devices [7, 70]. Nevertheless, a heater is still required to generate a thermal gradient in the sample, and its correct implementation is one of the main challenges for a functioning thermoelectric setup. The Corbino geometry also introduces an additional difficulty since the thermal gradient needs to be applied radially.

The task of finding an optimal solution for a heater compatible with sub 10 mK temperatures, high magnetic fields, Corbino geometry, and ultra-high mobility 2DEGs while avoiding substantial modifications of the current state of the device is tedious. Previous experiments [65–68] in the Corbino geometry employed various methods to generate a radial thermal gradient but were limited to temperatures higher than $\sim$ 300 mK. The approach from Ref. [65] using a focused laser spot to heat the center of the Corbino (see the inset of Fig.2.10a) is appealing since the device is not physically altered and the mobility would remain unaffected. However, it potentially creates a large source of heat leak for mK temperatures and also leads to ambiguous interpretations of the thermovoltage signal when considering the sensitivity of GaAs/AlGaAs heterostructures to light. The setup devised by Kobayakawa *et al.* [66] using radio frequency (RF) signals as a heat source (see the inset of Fig.2.10b) is also worth mentioning but raises concerns when applied to an ultra-high mobility sample. Finally, the most promising solution comes from recent works [67, 68] and is shown in the inset of Fig.2.10c. In their study, a Au/Pd micrometer-sized resistive heater film is patterned within the center contact of their Corbino sample. As a result, a radial thermal gradient is induced and the thermal contact and the thermal response time is excellent, allowing them to employ quasi-DC lock-in detection to measure thermoelectricity with a high degree of precision similar to previous works in the Hall bar geometry [62]. Although the authors did not measure their mobility with this setup, this configuration is in principle not detrimental to the sample quality since the heater is far away from the 2DEG rings where the transport is probed.

However, patterning an on-chip heater would require substantial modifications to the current device with photolithography, electron beam lithography, or even the fabrication of an entirely new device. Since we wished the device to remain unchanged in order to compare with previous results [55], a hybrid solution had to be considered. As a solution, we opted to heat the center contact of the Corbino device and create a radial thermal gradient in a similar fashion as Real *et al.* [67], with a heater in the form of a chip resistor glued to the center contact of the Corbino device.

3.2.2 Corbino device parameters

The ultra-high mobility Corbino device (CB05) is schematized in Fig.3.2a. It is based on a GaAs/AlGaAs heterostructure having a quantum well width of 30 nm, an electron density of $n_e = 3.08(1) \times 10^{11}$ cm^{-2}, and a measured mobility of $22(2) \times 10^6$ cm^2/Vs as reported in previous works on the same device [14, 53, 54]. The wafer (#3.11.10.2) was grown at Princeton university by L. N. Pfeiffer and K. West using state-of-the-art MBE. The contacts consist of Ge/Ni/Au layers patterned by photolithography. The inner circular contact has a radius of 0.25 mm, whereas the outer ring contact has an inner and outer radius of 1 mm and 1.5 mm, respectively. Further details pertaining to the fabrication and characterization of the device can be found in Ref. [14]. The contacts are wired with 25 μm gold wires soldered with indium. During the initial cooling process, the 2DEG was optimized by illumination with a red LED down to a temperature of ~ 5 K, a crucial process for the observation of the $\nu = 5/2$ FQH state.

3.2.3 Chip resistor heater thermoelectric setup

This chip resistor heater setup is quite simple in design and it is shown in Fig. 3.2a. It is glued to the center contact of the Corbino device with a thin layer of Apiezon N vacuum

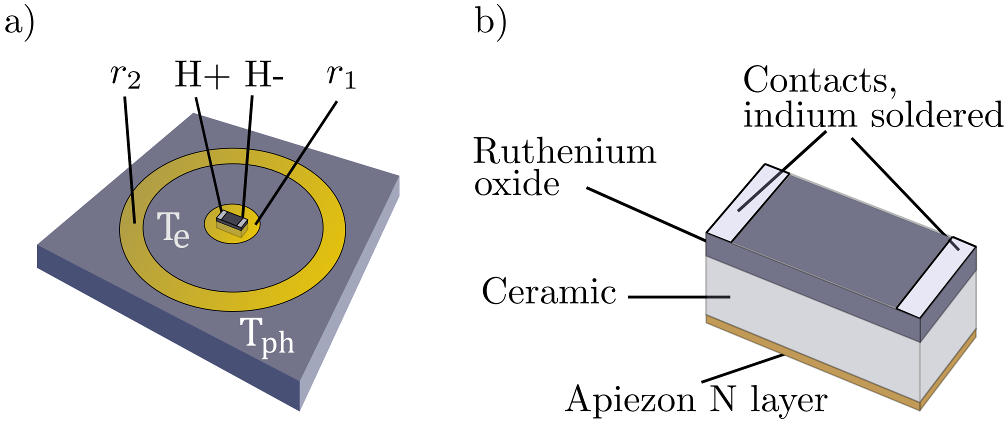

Figure 3.2: a) Schematic and pin-out of the Corbino device. The chip resistor heater is glued to the inner contact r_1 using a small layer of Apiezon N. The inner contact (r_1) has a radius of 0.25 mm and the outer contact (r_2) has a radius of 1 mm. H+ and H- are the chip resistor heater contacts. This configuration is identical for both CB01 and CB05 devices. b) Schematics of the chip resistor heater with a resistance of 200 Ω at room temperature and 374 Ω at 7 mK.

grease. This specific adhesive was selected for its thermal performance at low-temperature[5] and its ability to crystallize while cooling to base temperature, hence creating a solid thermal and mechanical bond with the center contact. The chip resistor is made of a ceramic substrate and a ruthenium oxide resistive element with metallic contacts as shown in Fig. 3.2b. This chip resistor was also selected to be as small as possibly available in order to maximally reduce its heat capacity. In this case, it has a length of 300 μm, a width of 150 μm and a height of 150 μm, which are dimensions compatible with the 500 μm diameter center contact.

To assess the suitability of the chip resistor setup as an efficient thermoelectric setup, the thermal response time was characterized by measuring the change in conductance following a heat pulse sent to the heater. The electrical circuit used to measure conductance as a function of magnetic field or heating power is shown in Fig. 3.3. A voltage V between the outer and inner contacts is set to 100 μV with a 1:1000 voltage divider and is measured with

---

[5] Even though at 100 mK Apiezon N has a rather low thermal conductivity 10^{-7} W/(cmK) compared to copper 10^{-1} W/(cmK), it creates a solid thermal link between two surfaces by filling the gaps of porous interfaces [72].

an SR830 lock-in amplifier. The current I is inferred by probing the voltage in a 1 kΩ resistor with a second SR830 lock-in amplifier synced to the same frequency as the previous lock-in amplifier. This frequency is typically 17.367 Hz throughout this work for quasi-DC transport measurements as a function of magnetic field but it can be varied and it will be stated when this is the case. Finally, the two-point conductance is calculated with $G = \frac{I}{V}$ and typically reported in units of μS. To extract the thermal response time of the chip resistor heater, the quasi-DC lock-in detection conductance circuit shown in Fig. 3.3 was slightly modified to allow for a much faster temporal resolution. Using an SR830 synced to a frequency of 17.367 Hz limits the temporal resolution to more than 300 ms because an average over a few cycles of 1/(17.367 Hz) is required to detect a consistent signal. To improve the temporal resolution, the SR830 was replaced by a HF2LI Zurich digital lock-in amplifier that can measure up to 50 MHz with 210 MSa/s. In that sense, employing a frequency of 123 kHz, a sampling rate of 124 kSa/s and a time constant of 100 μs was sufficient to resolve the time evolution of the conductance following the application of a square wave heating pulse of 1 μW, as shown in Fig. 3.4. The characterization of the thermal response time constant

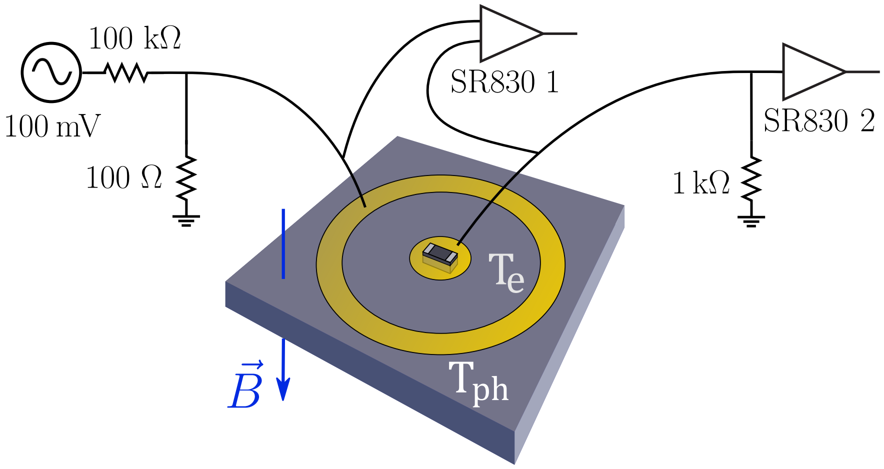

Figure 3.3: Circuit used to measure electrical transport and characterize the quantum Hall or fractional quantum Hall states within CB01 and CB05. In the limit of high impedance, the voltage across r_2 and r_1 is fixed to 100 μV by a 1/1000 potential divider. The voltage across the contacts is also measured with a lock-in amplifier whereas a second lock-in amplifier measures the current across a 1 $k\Omega$ resistor. Both lock-ins are synced to 17.367 Hz.

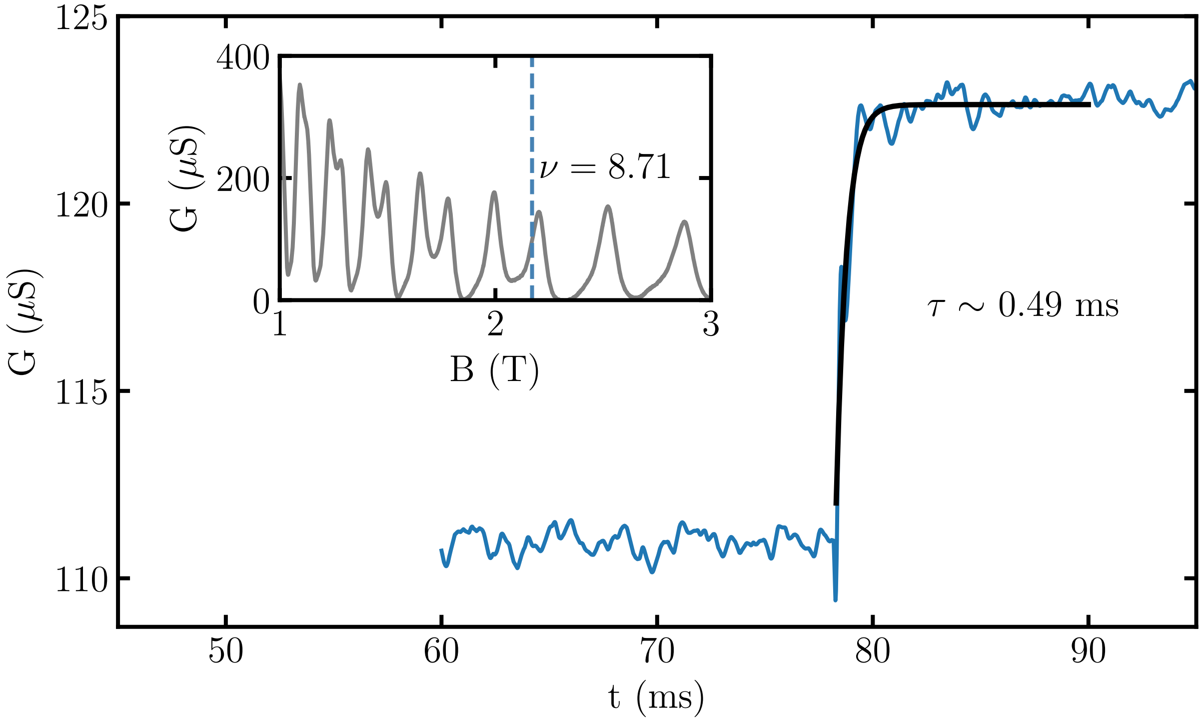

Figure 3.4: Thermal response time of the chip resistor heater measured using the change in conductance in device CB01. A 1 μW square wave is sent to the chip resistor heater and the conductance is measured using the circuit from Fig. 3.3 with the SR830 lock-in amplifier replaced by a HF2LI Zurich digital lock-in amplifier for faster data sampling. The signal is a result of an average over 92 samples. As shown in the inset, this was performed in the vicinity of the $\nu = 9$ IQH state where the conductance is highly dependent on temperature.

was performed in a lower mobility sample (CB01)[6] that has the exact same geometry as the ultra-high mobility device (CB05) at a filling factor in the vicinity of the $\nu = 9$ IQH state where the conductance is highly temperature dependent, as shown in the inset of Fig. 3.4. An exponential fit was employed to extract a thermal equilibration time constant of $\tau \sim 0.5$ ms, which is comparable to what was achieved in Ref. [9], allowing for lock-in detection at frequencies up to $\frac{1}{\tau} \sim 2$ kHz[7]. Considering that this was performed at a temperature of 10 mK and a magnetic field of around 2 T, it demonstrated that the chip heater resistor could be used for experimental conditions similar to where the $\nu = 5/2$ FQH state manifests. Additionally, earlier investigations of the electronic transport with the low mobility CB01

---

[6] This device has a mobility of 1.0×10^6 cm^2/Vs and a density of 4.6×10^{11} cm^{-2}.

[7] In practice, frequencies 10 or 100 times less than $\frac{1}{\tau}$ are selected to avoid phase shifts in ΔV [73].

device did not reveal significant degradation of its mobility. This will be further tested and discussed in chapter 4.

3.3 Thermopower measurement scheme

As defined in the section 2.3, one can experimentally access the longitudinal thermopower S_{xx} by probing separately the thermovoltage ΔV_{rms} and the thermal gradient ΔT_{rms}, and then computing the thermopower given by

$$S_{xx} = -\frac{\Delta V_{\mathrm{rms}}}{\Delta T_{\mathrm{rms}}}, \tag{3.2}$$

where a distinction from eq. (2.9) is made in regard to the root mean square (RMS) values which are the experimentally accessible quantities using a lock-in detection technique.

3.3.1 Measurement of the thermovoltage

Owing to its low Seebeck coefficient (S_{xx}), which was reported previously [9] to be on the order of ~ 0.1 μV/K for the $\nu = 5/2$ FQH state, thermovoltage signals of a few nV are expected for temperature gradients of a few mK. Therefore, the thermovoltage measurement circuit must be sensitive enough to detect sub-nV signals. This was realized by using a SR560 low-noise voltage pre-amplifier to amplify signals before the SR830 lock-in detection stage as shown in Fig. 3.5a. The SR560 has an input noise of 4 nV/$\sqrt{\mathrm{Hz}}$ at 1 kHz[8] and an input impedance of 100 MΩ, making it adequate for measuring nV signals in the $\nu = 5/2$ FQH state where the impedance of the device reaches ~ 5 MΩ. Even though the instruments used to detect the thermovoltage signal are quite straightforward, the interpretation of the signal on the lock-in channels requires more analysis to be converted to thermovoltage. First, as seen in Fig. 3.5a, the SR830 lock-in amplifier drives a sinusoidal waveform $\sin(\omega t)$ to the heater

---

[8] The input voltage noise increases to 5 nV/$\sqrt{\mathrm{Hz}}$ at 80 Hz, close to 2ω where the measurements are performed.

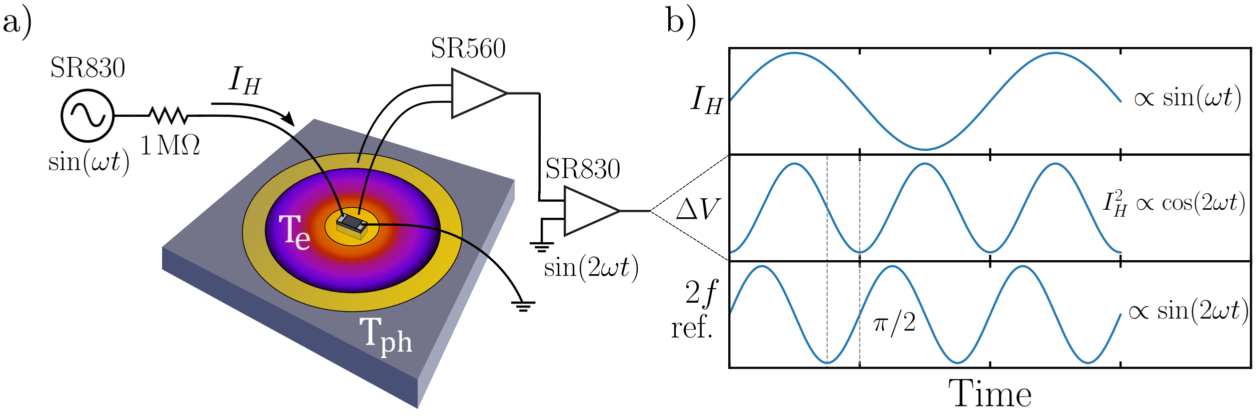

Figure 3.5: a) Schematic showing the measurement circuit employed to measure quasi-DC thermovoltage using the chip resistor setup. b) Representation of the heater current I_H, the thermovoltage ΔV, and the lock-in reference at 2ω in the time domain.

via a 1 MΩ resistor in order to fix the current to $I_H = I_0 \sin \omega t$.[9] As a result, the heating power $\dot{Q}_{\mathrm{rms}}$ from Joule heating occurs at twice the frequency of the heater current

$$\dot{Q}_{\mathrm{rms}} = R_H I_H^2 = R I_0^2 \sin^2 \omega t = \frac{R I_0^2}{2} \left(1 - \cos(2\omega t)\right). \tag{3.3}$$

This is shown schematically in Fig. 3.5b and also demonstrates that the thermovoltage will be in phase with the resulting thermal gradient induced at $\cos(2\omega t)$. Therefore, the thermovoltage is lock-in detected at the second harmonic 2ω in the Y channel since $\cos(2\omega t)$ is $\pi/2$ out of phase with respect to the original $\sin(\omega t)$ signal. In addition, from this circuit configuration, no signal at ω should be detected, and the signal at 2ω should change sign upon inversion of the probes and be monotonic with respect to $\dot{Q}_{\mathrm{rms}}$.

3.3.2 Determination of the temperature gradient

The crucial component to get an accurate absolute measurement of the Seebeck coefficient S_{xx} is to induce a known temperature gradient ΔT_{rms} between the device contacts. This is challenging to achieve in the Corbino geometry since the resulting gradient is by nature

---

[9] For the experiments performed in this work, the current typically ranges between 0 and 5 μA, yielding a heating power ranging approximately from 0 to 10 nW.

non-linear as a function of r and must be uniform with respect to θ. This was attempted in earlier works [67, 68] but the induced ΔT was estimated with theoretical modeling instead of using a calibration. The procedure described here in Fig. 3.6 is analogous to the *in-situ* method implemented by previous works in Hall bars [7, 9, 62, 70], although it is adapted for the Corbino geometry. The ΔT_{rms} calibration procedure relies on the strong temperature dependence $G(T)$ of the conductance as an *in-situ* thermometer near FQH states as shown in Fig. 3.6b. As such, an electron temperature calibration is first performed by varying the temperature of the mixing chamber and device from T_0 to T_1 and recording the resulting $G(T)$ curve. Then, the heating power $\dot{Q}_{\mathrm{rms}}$ of the heater is incremented until the conductance[10] is equal to $G(T_1)$, implying that the average electron temperature $\langle T_e \rangle$ is equal to T_1. The

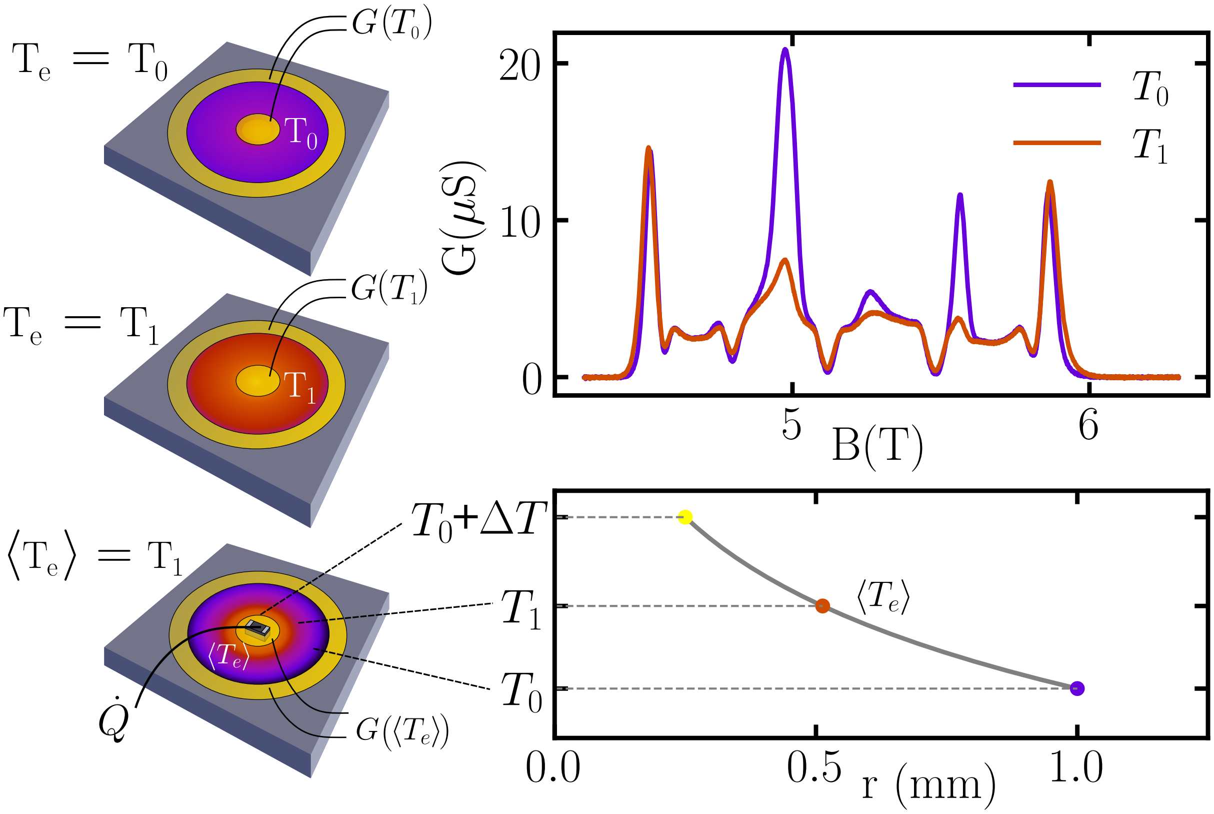

Figure 3.6: Schematic of the procedure to apply and measure a known thermal gradient ΔT between the device contacts.

---

[10] The conductance measurement is a spatial average of the conductance from r_1 to r_2, and thus provides information on the average temperature of the 2DEG regardless of the temperature gradient.

heating power $\dot{Q}_{\mathrm{rms}}$ can thus be related to the average temperature of the 2DEG, and it is in turn linked to the thermal gradient ΔT_{rms} by the following relation,

$$\Delta T_{\mathrm{rms}} = \frac{\langle T \rangle - T_0}{1 - \frac{r_1 \log \frac{r_2}{r_1}}{r_2 - r_1}} = 1.86 \left(\langle T \rangle - T_0 \right), \tag{3.4}$$

where r_1 and r_2 are the radii of the device contacts as defined in Fig. 3.2 and T_0 is the temperature of the device before applying heat. This result is derived in appendix B and deviates from the expected $\Delta T_{\mathrm{rms}} = 2 \left(\langle T \rangle - T_0 \right)$ for a Hall bar since the thermal gradient is a logarithmic function of r as a result of heat diffusion in the Corbino geometry. Modeling of $T(r)$ using the heat equation in the Corbino geometry is shown in Fig. 3.6. To extract an accurate value for ΔT_{rms}, the calibration process is repeated for multiple T_0 temperatures and filling factors ν because *a priori*, the response of the device to heat (thermal conductance) is not the same for all filling factors in the vicinity of FQH states as shown in Ref. [74] and $\Delta T_{\mathrm{rms}}(\nu, T_0)$ could be a function of ν. In that sense, one needs to record the conductance $G(\nu, T_0, \dot{Q}_{\mathrm{rms}})$ at each filling factors ν, temperatures T_0 and heating power $\dot{Q}_{\mathrm{rms}}$.

Another noteworthy difficulty is selecting a temperature gradient small enough to remain in the linear regime of the longitudinal thermopower since S_{xx} depends on temperature. In previous studies in GaAs [7, 9, 62], temperature gradients of less than 10% of the initial temperature T_0 were selected to ascertain the linearity. However, in another recent work in bilayer graphene [63], the authors pushed that limit to 35% and claimed to remain in the linear regime. Altogether, the ideal case is the limit when $\dot{Q}_{\mathrm{rms}}, \Delta T_{\mathrm{rms}} \to 0$, which inevitably becomes hard to achieve as the temperature is lowered towards ~10 mK.

Chapter 4

Results and discussion

In this chapter, the electronic transport of the ultra-high mobility Corbino device is first investigated prior to installing the chip resistor heater. The thermovoltage signal is then validated as being a genuine thermoelectric voltage based on multiple experimental assessments and by comparing its transport properties in the QHE and FQHE with expectations in the Corbino geometry. A temperature gradient calibration is performed at multiple partial filling factors ν^* in the vicinity of the $\nu = 5/2$ FQH state. Here, as is the norm in the FQH literature, partial fillings ν^* are defined as a deviation $\nu^* = \nu - \nu_0$ from the exact filling factor ν_0 of a given FQH state. Finally, the apparent degradation of the 5/2 FQH state by the chip resistor heater is tentatively explained in terms of potential thermal-contraction-induced strain mechanisms that could have lowered its energy gap.

4.1 Electronic transport and benchmarking of fractional quantum Hall states

Before the chip resistor heater setup was implemented and any thermoelectric measurements were attempted, the ultra-high mobility Corbino device (CB05) was characterized with electronic transport measurements in the SLL using the conductance circuit shown in Fig. 3.3. This was compared to earlier data from a previous study [55] in the same device in 2020 and it is shown in Fig. 4.1. Both data sets were acquired in the same dilution refrigerator at the same base temperature of 7 mK, however with sample stages of different design. During cooldown to base temperature, the device was illuminated with a red LED until a temperature of ~ 5 K to optimize the electron mobility and density.

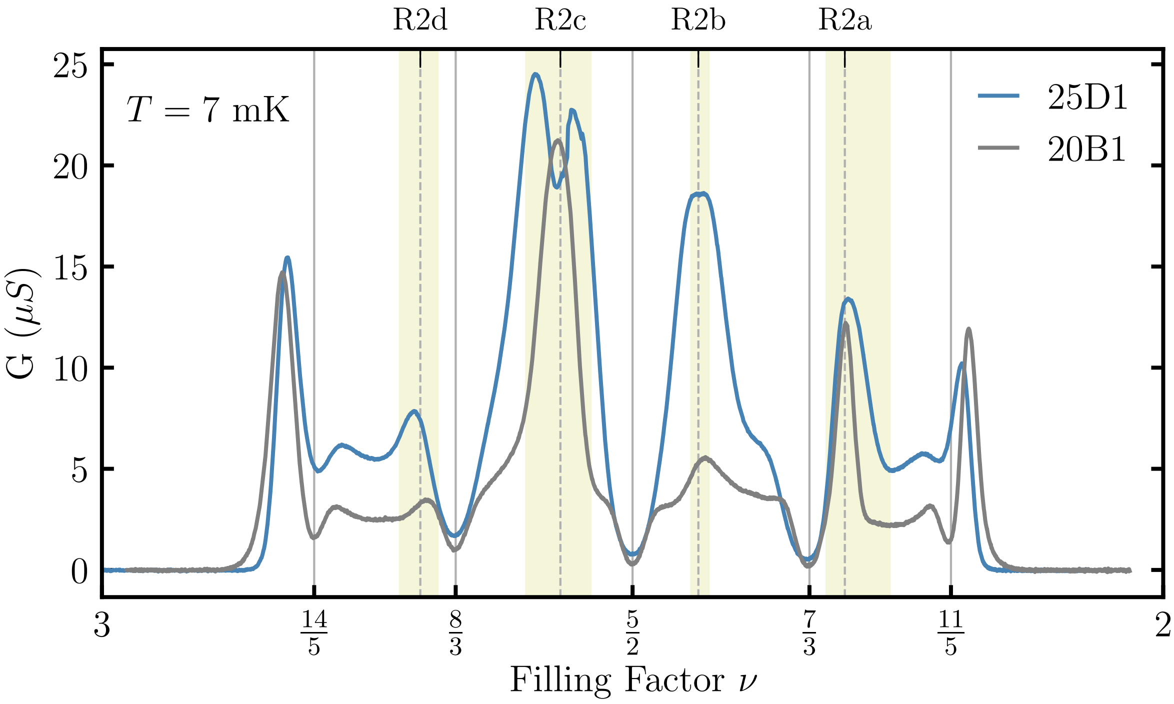

Figure 4.1: Bulk electrical conductance as a function of filling factor in the SLL, where the most well-developed FQH and RIQH states are indicated respectively by solid and dashed grey lines. The two data sets were acquired 5 years apart where 20B1 and 25D1 respectively stand for cooldown number B1 in 2020 and cooldown number D1 in 2025.

Both data sets show a high-quality electronic transport in the SLL with multiple visible features such as the $\nu = 11/5,\ 7/3,\ 5/2,\ 8/3$, and $14/5$ FQH states and several reentrant integer quantum Hall (RIQH) states, *i.e.* R2d, R2c, R2b, and R2a. These peculiar states typically manifest as integer plateaus in R_{xy} (*e.g.* $h/3e^2$ for R2d and R2c, and $h/2e^2$ for R2b and R2a) even though they occur at non-integer filling factors. Hence, they are a hallmark of the 2DEG quality and the thermalization quality since they develop at low temperatures and have a non-monotonic temperature dependence [75]. For instance, the conductance for the R2c reentrant integer quantum Hall (RIQH) state first increases with decreasing temperature and then sharply collapses to $G \to 0$ as T is further lowered. In this case, see Fig. 4.1, the presence of a dip at the R2c state in the recent 2025 (25D1) data set could be attributed to a lower electronic temperature than the previous 2020 (20B1) data set where the peak at R2c is suggestive of a less developed RIQH state.

However, another possibility for the dip in R2c is an in-plane field enhancement which is known to be favorable to some states while being detrimental for others [76]. For the 2025 (25D1) data, the device was slightly off-centered in the z axis of the magnetic field by 20 mm because the G10 post piece missing at the time of the measurement and the device was placed directly on the sample stage bottom plate (see Fig. A.1 of appendix A). This resulted in an overestimation of the perpendicular magnetic field in z by $\sim 1.25\%$ and an in-plane field of ~ 170 G. Thus, some of the data reported here, namely in Figs. 4.2, 4.4, 4.5, and 4.7, was acquired in this non-ideal off-centered configuration, however it was later corrected by adding the properly designed G10 post piece.

Regardless of the apparent quality of the 2DEG deduced from the transport measurement in the SLL, the energy gap Δ is more revealing as it relates to the electron mobility, and provides a figure of merit for the robustness of the FQH many-body state [77]. This energy gap was extracted for the $\nu = 5/2$ FQH state and compared to earlier values in the same device as shown in Fig. 4.2b. A gap of 114(5) mK was determined using the Arhenius relation $G = G_0 e^{-\Delta/2k_BT}$, which is smaller than the previously measured gap of 172(5) mK in the same device. It is unclear whether this was due to the small in-plane magnetic field, a degradation of the device mobility or simply an inaccuracy in the measurement itself. The latter is more plausible since there is a visible outlier and significantly fewer data points were acquired. This issue will be addressed in more detail later with subsequent measurements

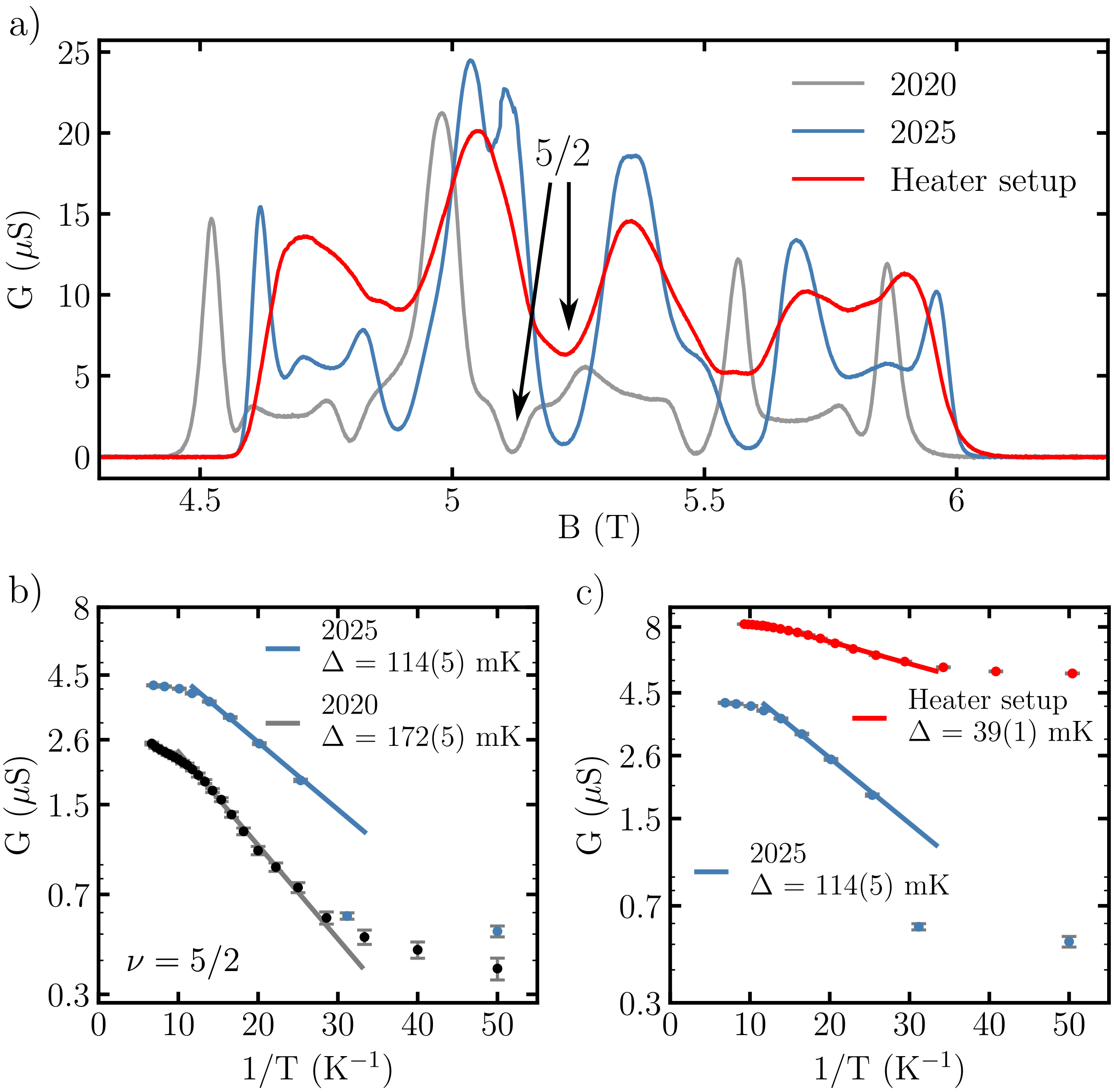

Figure 4.2: a) Comparison of the transport in the SLL after installation of the chip resistor heater setup on device CB05. b) Arrhenius plot of the conductance as a function of temperature in order to extract the gap of the $\nu = 5/2$ state. c) Energy gap of the $\nu = 5/2$ with the chip resistor heater installed on the device.

where the device was located exactly in the center of the field (see Fig. 4.10c at the end of chapter 4). While both energy gaps are lower than previously reported in similar ultra-high mobility devices [31], where a gap of ∼450 mK was determined, it is not an issue in our case for measuring a possible non-Abelian entropy since an electron temperature below 20 mK is still much lower than the 5/2 FQH energy gap, $\Delta_{5/2} = 114(5)$ mK.

Unfortunately, the situation differed sharply when the chip resistor heater was installed on the center contact of the device. The quality of the high-mobility Corbino device was again assessed with electronic transport and energy gap measurements, and these are reported in Figs. 4.2a,c, where the most sensitive FQH states ($\nu = 11/5,\ 14/5$) are no longer noticeable. Additionally, the gap of the 5/2 FQH state is now suppressed down to 39(1) mK, and this is highly detrimental for probing non-Abelian entropy since the experimental temperatures are now comparable to the FQH energy gap, *i.e.* the quasiparticles are now thermally excited. Possible explanations for this degradation of the quality of the device will be discussed later in this chapter. In spite of this major setback, the chip resistor heater setup was tested and the thermopower was studied in this non-ideal regime to gain experimental insights. This is discussed in the remaining sections of this chapter where the thermoelectric signals are characterized in both the QHE and FQHE regimes of the Corbino device.

4.2 Thermovoltage signal characterization

4.2.1 Thermovoltage circuit properties assessment

Several validations were performed to assess that the thermovoltage circuit shown in Fig. 3.5 gives physical values consistent with thermoelectricity. This first validation consists in verifying that there is no electrical short circuit from the heater leads to the center contact of the device. This was done routinely at the beginning of each cooldown and typical values are reported in table C.1 of appendix C. All the validations presented in Fig. 4.3 were performed in the vicinity ($\nu^* = 0.01$) of the $\nu = 5/2$ FQH state where the thermopower signal is large, except for Fig. 4.3c (at $\nu^* = 0$).

To first verify that the chip resistor is effectively heating the 2DEG, the conductance at the 5/2 minimum was recorded as a function of the heater current I_{heat} from -5 to 5 μA as shown in Fig. 4.3c. Since $G_{5/2}$ is a monotonic function of T, this reveals that the average temperature of the 2DEG increases with $\pm I_{\text{heat}}$. Although there is a significant

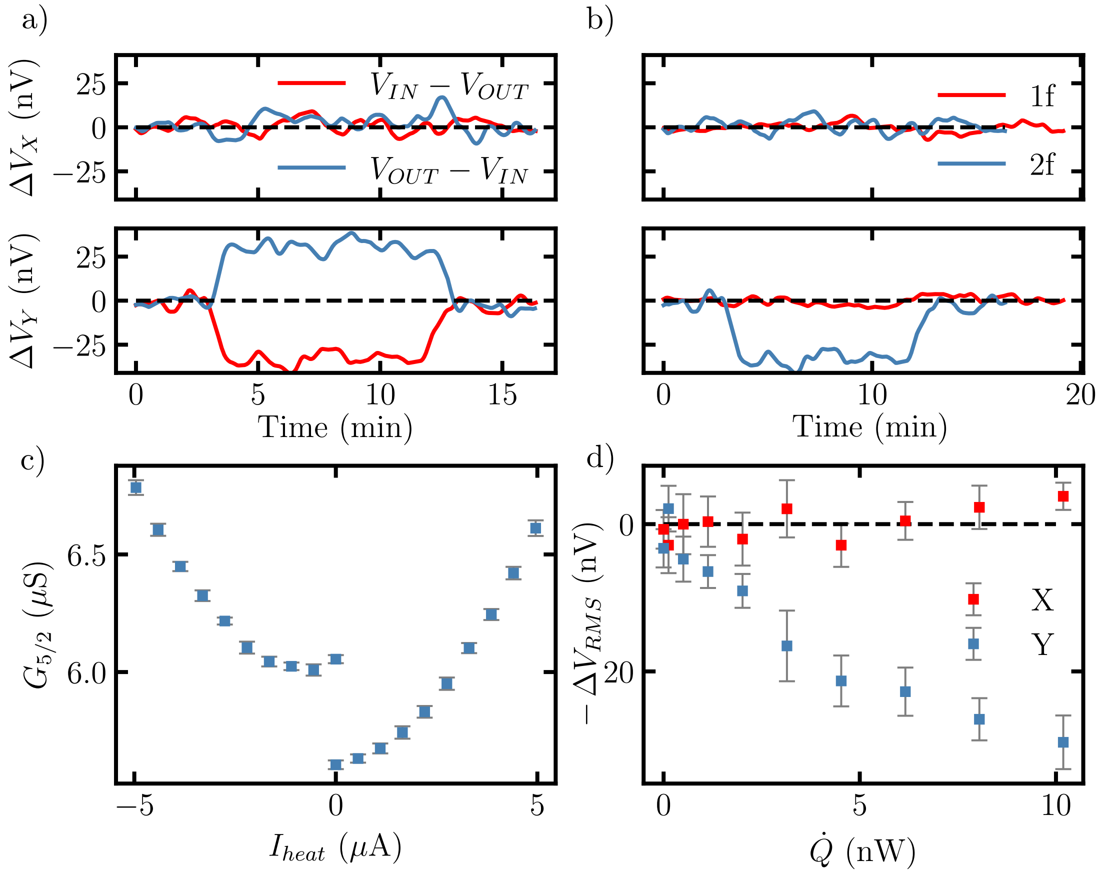

Figure 4.3: a) Voltage detected at $2f$ in the X and Y channels with two inverted probes configurations. b) Voltage detected at $1f$ and $2f$ in the X and Y channels. c) Electrical conductance as a function of heating current sent in the chip resistor at $\nu = 5/2$. d) Voltage detected at $2f$ in the X and Y channels as a function of heater power.

asymmetry from $\pm I_{\text{heat}}$, that arises from an insufficient thermal relaxation time to base temperature between the $+I_{\text{heat}}$ and $-I_{\text{heat}}$ data sets, the parabolic shape is consistent with Joule heating, *i.e.* $G \propto \dot{Q} = R_H I_{\text{heat}}^2$, where R_H is the resistance of the heater. In this respect, the conductance is linear with I_{heat}^2 as is expected from Joule heating and as is observed in Fig. C.1 of appendix C.

Based on the design of the thermovoltage circuit, the thermoelectric signal is expected among others to; (i) change sign upon inversion of the voltage probes, (ii) be exclusively in the Y channel at $2f$, and (iii) be linear with heating power in the low-power limit. These properties are all respected, as shown in Figs. 4.3a,b,d. This also rules out any possible current leaking from the heater to the 2DEG since otherwise a large signal would have been detected at $1f$. Additionally, the measured thermovoltage is independent of frequency below ~ 50 Hz, *i.e.* far away from the limit set by the thermal response time of the heater[1], as shown in Fig. E.1 of appendix E. Thus, the frequency-independent signal guarantees that the magnitude of the thermovoltage is not distorted by phase shifts from a slow thermal response.

These validations demonstrate that the voltages measured with the chip resistor heater setup shown in Fig. 3.5 are genuine *thermovoltage* signals. Nonetheless, in the next section, we will show with transport measurements in the IQHE regime that this thermovoltage is also consistent with longitudinal diffusion thermopower in the Corbino geometry.

4.2.2 Thermovoltage in the quantum Hall effect regime

As shown in Fig. 2.9, in the QHE regime, the longitudinal Hall bar and Corbino thermopower contrast sharply. This was first pointed out in the theoretical work of Barlas and Yang [8], as it gives rise to a *saw tooth pattern* that oscillates between positive and negative values at integer filling factors.

These features are observed in Fig. 4.4 in the regime where the IQHE begins to undergo spin-splitting, *i.e.* where the Zeeman energy splits the electron spin degeneracy in LLs. As highlighted in yellow, between two LLs and at the center of a LL, the thermovoltage vanishes and changes sign concomitantly with a conductance minimum. This indeed provides a confirmation that the thermoelectric voltage measured here originates from Corbino longitudinal diffusion thermopower. Note that no temperature calibration was performed in this regime and that a fairly large heating power was used, *i.e.* $Q_{\mathrm{rms}} = 10$ nW, in order to increase the thermovoltage signal and make a clear observation of the expected saw tooth pattern. Consequently, ΔV_{rms} could not be converted to S_{xx} since in this case the thermal

---

[1] The thermal response time was estimated to be 0.5 ms (see Fig. 3.4), which sets a limit of $2f = 2$kHz on the frequency before encountering phase shifts from an insufficient thermal relaxation time.

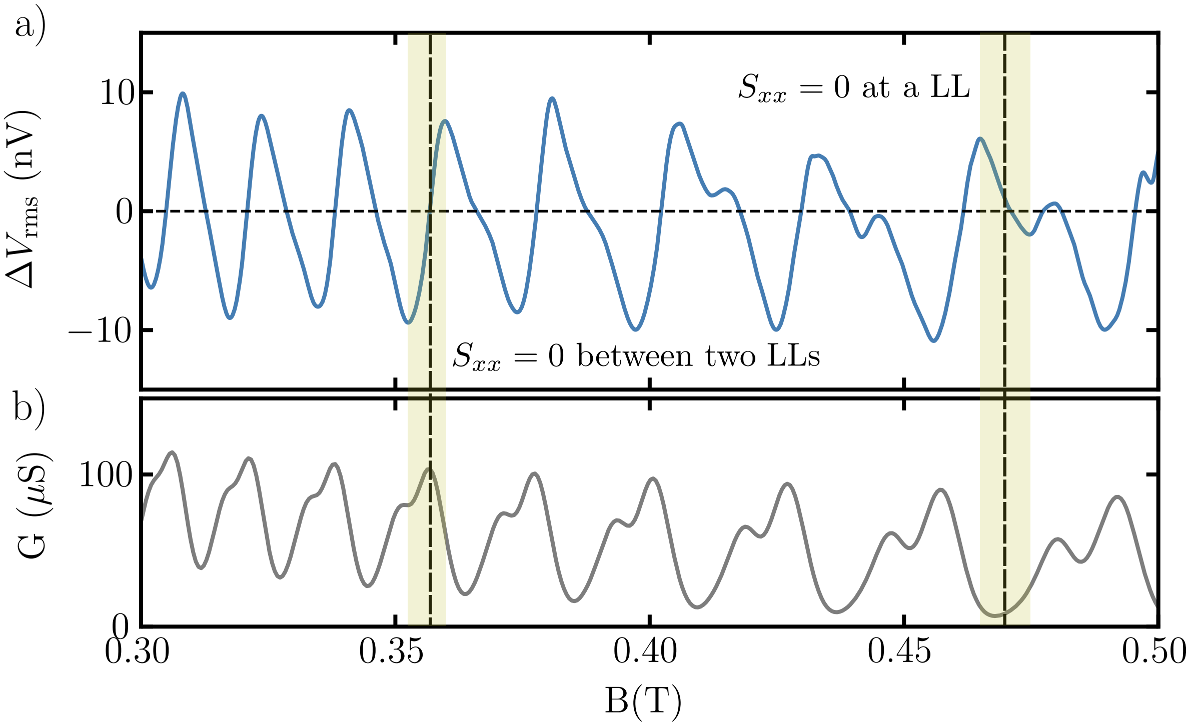

Figure 4.4: a) Thermovoltage in the spin-splitting regime of the QHE for an applied heating power of $Q_{\rm rms} = 10$ nW. b) Electrical conductance at the same magnetic fields as in a).

gradient $\Delta T_{\rm rms}$ is unknown.

Probing the thermovoltage in the IQHE regime at higher magnetic fields (lower LLs) proved to be more difficult and yielded incoherently large fluctuating signals at integer filling factors as seen in Fig. 4.5a. However, the expected sign reversal from Corbino thermopower is still observed in-between LLs, as shown by Fig. 4.5b, where large spurious signals were artificially removed. Surprisingly, this behavior is not new and has been observed before albeit to a smaller extent in previous works in the Corbino geometry [67]. In this work [67], the authors attributed these large spurious signals to *temperature-driven magnetic flux or temperature-dependent contact potentials that cannot equilibrate in the conductance minima*. However, the latter is here implausible since it has been experimentally shown that the bulk of IQH states remain thermally conductive even in the conductance minima [74,78]. Another noteworthy origin for these large signals could be an experimental artifact caused by the bulk insulating IQH states, whereby the impedance between the voltage probes exceeds the input impedance of the pre-amplifier. If this is the case, it would explain why the effect is stronger in our work since a 100 MΩ input impedance pre-amplifier was used rather than the 1 TΩ input impedance pre-amplifier used in the work of Ref. [67].

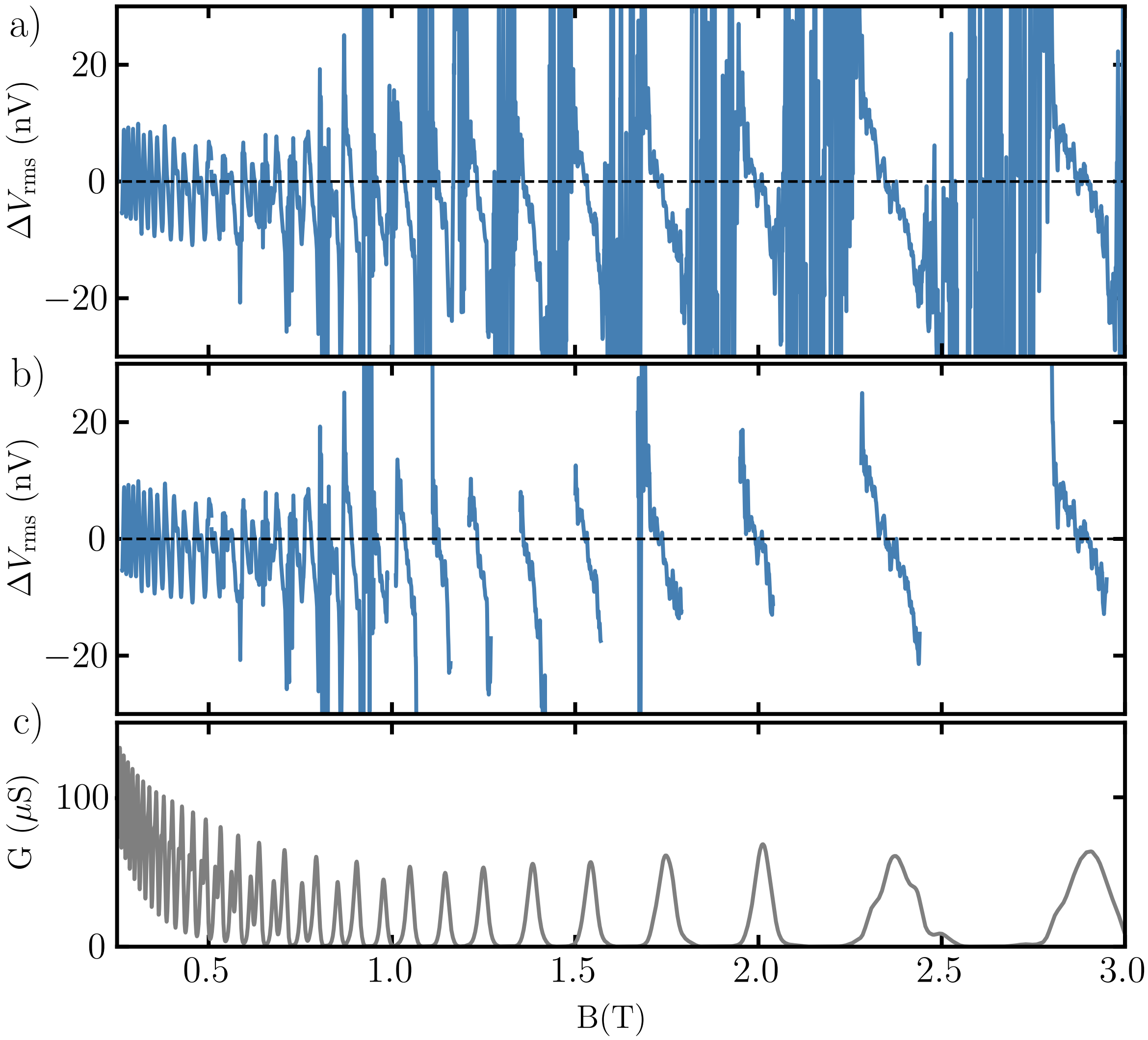

Figure 4.5: a) Raw thermovoltage in the QHE regime for an applied heating power of $Q_{\rm rms} = 10$ nW. b) Thermovoltage in the QHE in which the unphysical signal when $G \to 0$ is removed. c) Electrical conductance at the same magnetic fields as in a) and b).

For the same reasons as for the data shown in Fig. 4.4, no temperature calibration was attempted and as a result no absolute thermopower could be extracted from the signal measured in Fig. 4.5. This fact, combined with the much higher base temperature of $\sim$ 300 mK in Ref. [67], hinders a precise quantitative comparison of the magnitude of the thermovoltage between their and our work. Nonetheless and remarkably, the amplitude of the thermovoltage for similar IQH states is on the same order of magnitude, *i.e.* ~ 20 nV for this study compared to ~ 100 nV for Ref. [67].

Finally, regardless of the thermovoltage magnitude and the spurious signals observed, the *saw-tooth*-sign-change behavior is consistent with Ref. [67]'s work and with theoretical modeling [8], providing further confirmation that indeed the measured voltage originates from Corbino longitudinal diffusion thermopower. In the next section, we will focus on extracting the thermopower S_{xx} in the vicinity of the 5/2 FQH state using a proper temperature calibration procedure in an effort to determine the temperature gradient.

4.3 Determination of a fixed temperature gradient

First, we note that measuring thermovoltages alone is not sufficient to shed light on the non-Abelian nature of the $\nu = 5/2$ FQH state since it is necessary to perform a temperature calibration to extract an accurate value for the temperature gradient (ΔT), as detailed in Fig. 3.6. This is presented in Fig. 4.6 at three partial filling factors ν^* in the vicinity of $\nu = 5/2$, namely, $\nu^* = -0.01,\ 0.00$, and 0.01. As a first step, the temperature dependence of the conductance was measured at each ν^* and these are reported in Fig. 4.6a. Secondly, the conductance as a function of heating power $\dot{Q}_{\mathrm{rms}}$ was measured at base temperature and they are shown with shared axes in Fig. 4.6b, for clarity. Then, the conductance was converted to the average electron temperature $\langle T_e \rangle$ versus $\dot{Q}_{\mathrm{rms}}$ using the previously measured $G(T)$ data and this is shown in Fig. 4.6c. Here, the lowest $\langle T_e \rangle$ achieved was approximately 20 mK for $\nu^* = 0.01$ and $\nu^* = 0$, and 15 mK for $\nu^* = -0.01$. This lower bound was estimated from the saturation of the $G(T)$ curve at low temperatures. Finally, for a heating power of 0.66 nW, which was selected for later measurements in the vicinity of the $\nu = 5/2$ FQH state, the average temperature was translated to ΔT_{rms} as a function of ν^* and this is shown in Fig. 4.6d. The $\dot{Q}_{\mathrm{rms}}$ was selected to be 0.66 nW in order to obtain a sufficiently strong

S_{xx} signal while remaining linear with respect to $\dot{Q}_{\mathrm{rms}}$.

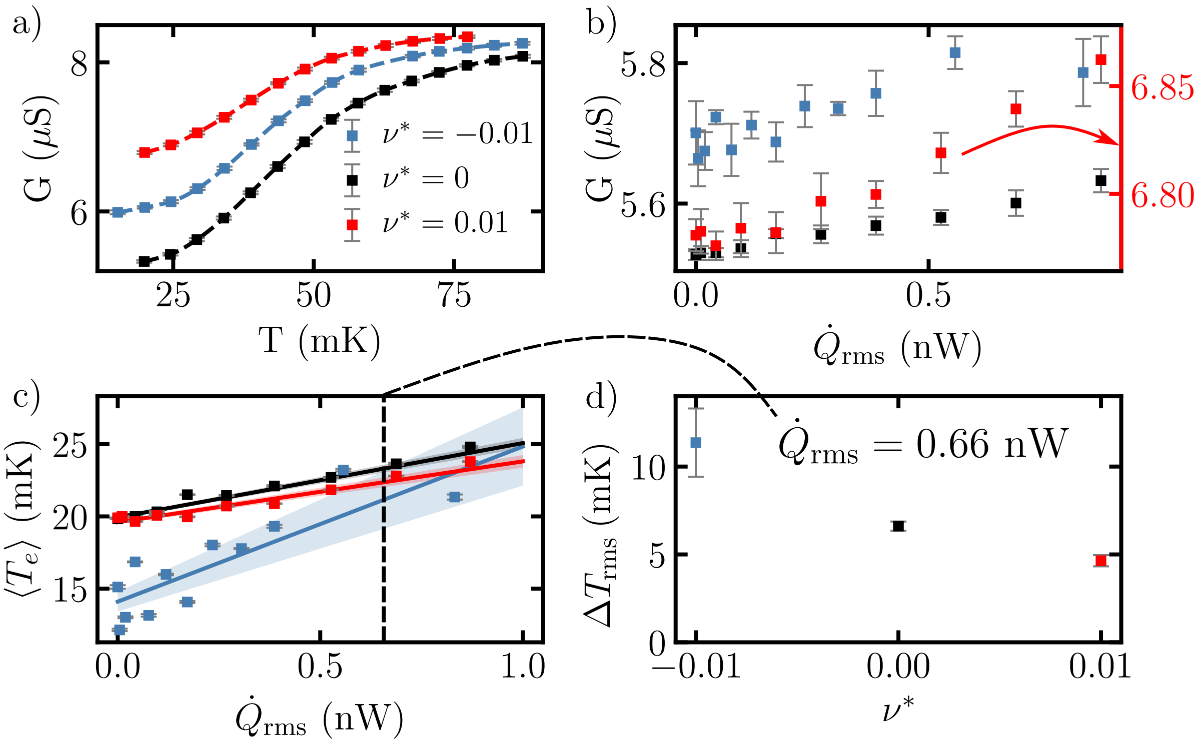

Figure 4.6: Temperature calibration at multiple ν^* in the vicinity of the $\nu = 5/2$ FQH state. The points where the calibration is performed are shown in Fig. 4.9 as stars points. a) Conductance versus temperature in the vicinity of the 5/2 FQH state for multiple ν^*. An interpolation is performed and shown as a dashed line. b) Conductance versus RMS heater power at the same partial filling factors. c) Average temperature of the 2DEG vs RMS heater power. The solid line is a linear fit. d) Extracted temperature gradient ΔT_{rms} as a function of filling factor for a $\dot{Q}_{\mathrm{rms}} = 0.66$ nW heater power.

As seen in Fig. 4.6d, the temperature gradient is not constant as a function of filling factor, although more data points are needed to get a definitive picture. In short, it means that in the Corbino geometry, it is essential to extract the full matrix of data points, *i.e.* $\Delta T_{\mathrm{rms}}(T_0, \nu^*, \dot{Q}_{\mathrm{rms}})$, and to get accurate values of the longitudinal diffusion thermopower at each $(T_0, \nu^*, \dot{Q}_{\mathrm{rms}})$ points. Nevertheless, these results are useful for a preliminary exploration of S_{xx} and to gain insights on the magnitude of the expected parameter space as a function of $(T_0, \nu^*, \dot{Q}_{\mathrm{rms}})$. For example, at $\dot{Q}_{\mathrm{rms}} = 0.66$ nW and for $\nu^* = 0.01$ and $\nu^* = 0.00$, the temperature gradient $\Delta T_{\mathrm{rms}} < 30\%\ T_0$, which indicates that the measurement is in agreement with the linearity threshold set by Ref. [63], *i.e.* the temperature gradient must not exceed 35% of the base temperature T_0. For these two filling factors, falling below this threshold means that the estimate for S_{xx} should be accurate. However, for a power of $\dot{Q}_{\mathrm{rms}} = 0.66$ nW, the linearity threshold was not respected for $\nu^* = -0.01$ indicating that S_{xx} should be measured at an even lower $\dot{Q}_{\mathrm{rms}}$. Finally, as an additional confirmation that the temperature calibration provides meaningful insights, the heating power required to achieve a given temperature gradient was found to be on the same order as therein Refs. [7,9,62] for similar temperatures.

4.4 Thermopower in the fractional quantum Hall effect regime

4.4.1 Thermopower in the second Landau level

Now equipped with a procedure to estimate the temperature gradient, an estimation of the absolute thermopower S_{xx} can now be made. First, a measurement of S_{xx} as a function of the magnetic field was performed in the SLL, and this is shown in Fig. 4.7. For this data set, the temperature calibration and the data acquisition was performed at $\nu^* = -0.01$ in an earlier cooldown where the device was slightly out of the field center (see Fig. D.1). Since the objective was to clearly observe the features in S_{xx}, a higher temperature gradient of 20(1) mK ($\dot{Q}_{\mathrm{rms}} = 1.25$ nW) was selected to obtain a stronger signal, unfortunately at the cost of violating the linearity threshold of $< 35\%\ T_0$ and potentially degrading the accuracy of the quantitative value of S_{xx}. A behavior reminiscent of the longitudinal diffusion Corbino thermopower similar to the IQHE case (see Fig. 4.4) is found, as can be seen in Fig. 4.7, where S_{xx} vanishes and changes sign at, and in-between FQH states highlighted by the yellow shaded regions. This sign change is expected again for FQH states since S_{xx} is a probe of *entropy per quasiparticle per quasiparticle charge*, as first pointed out by Barlas and Yang in the Corbino geometry [8]. In fact, S_{xx} changes sign as the transport switches from

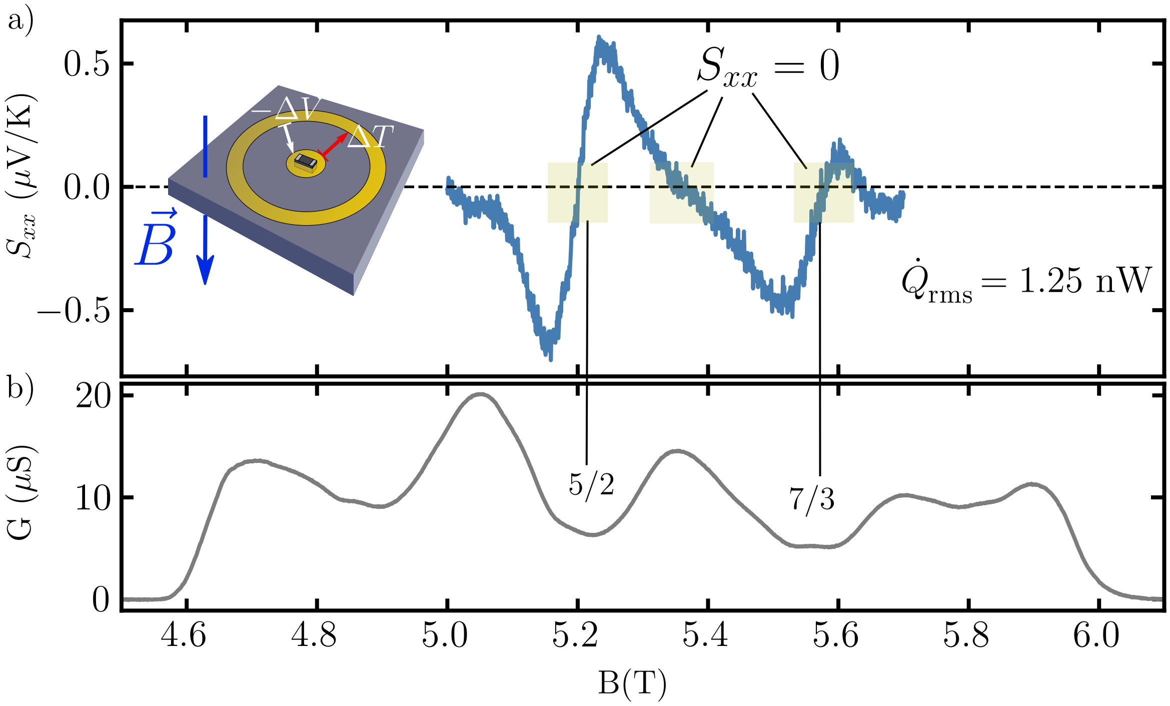

Figure 4.7: a) Thermopower in the SLL as a function of magnetic field. Inset showing the direction of the magnetic field, the thermal gradient and the thermovoltage. b) Corresponding electrical conductance at the same magnetic fields.

quasiparticle to quasihole dominated, as this is consistent with the nature of the transport described by eq. (2.14). For partial filling factor $\nu^* < 0$ ($B > B_0$), S_{xx} is positive in the quasiparticle transport region to the right of the 5/2 state center (B_0), and alternatively, it is negative for the quasihole $\nu^* > 0$ ($B < B_0$) region. At first, this might seem inconsistent with the sign of the quasiparticle charge e^*, but we note that the magnetic field in our experiment was pointing down, ultimately demonstrating that the proper sign of S_{xx} was observed (see the inset of Fig. 4.7 and see Fig. 4.8).

4.4.2 Thermopower in the $\nu = 5/2$ FQH sstate

Following having gained understanding of the thermopower signal in the QHE and FQHE regimes, a quantitative measurement of S_{xx} in the $\nu = 5/2$ FQH state was performed symmetrically with respect to the center B_0 of the state between $\nu^* = -0.01$ to $\nu^* = 0.01$ as shown in Fig. 4.8. Here, the thermovoltage data was converted to S_{xx} using the temperature calibration performed at $\nu^* = 0.01$ in accordance with the linearity threshold at $\dot{Q}_{\text{rms}} = 0.66$ nW, and this is shown in a shared axis with electronic conductance for clarity. The quasihole and quasiparticle regions are separated by a gray dashed line, and the sign of the effective charge e^* is indicated. Even though the uncertainty relative to the signal is large, a clear sign change in S_{xx} consistent with e^* is observed in the vicinity of B_0 and this is in clear agreement with an *entropy per quasiparticle per quasiparticle charge* (eq. (2.14)) interpretation of thermopower in the Corbino geometry.

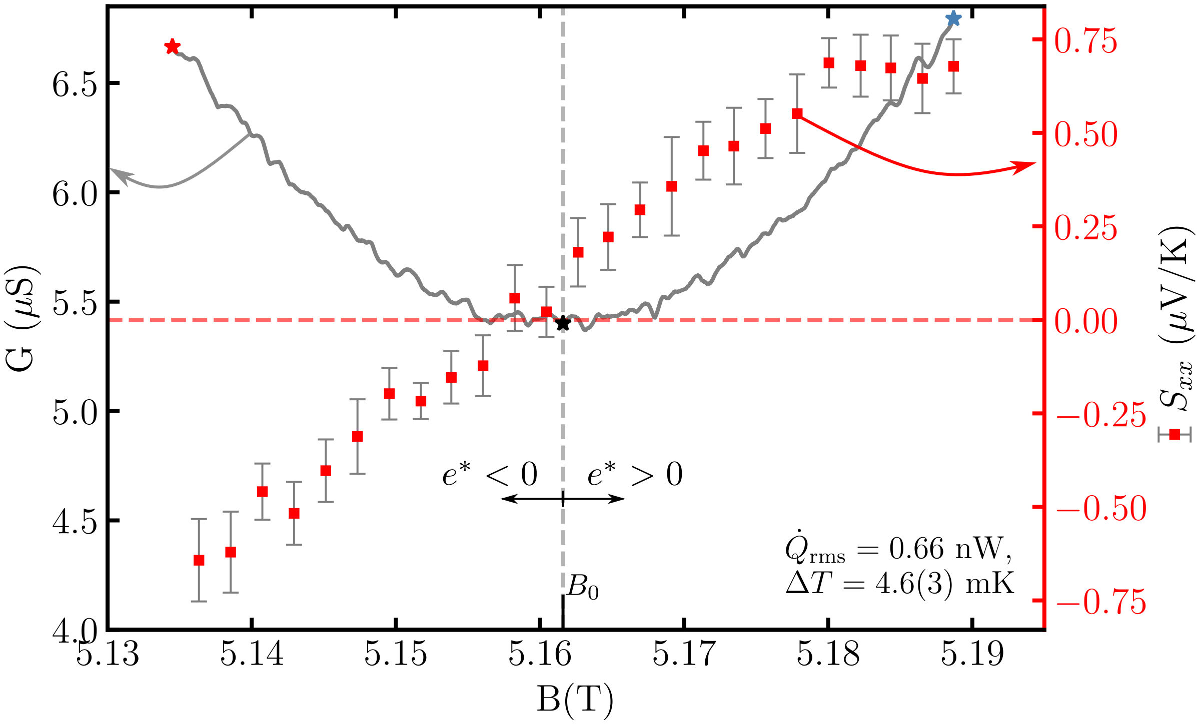

Figure 4.8: Thermopower at $\nu = 5/2$ filling factor shown on shared axis with the conductance. Each data points is averaged over five minutes. The red star point indicates where the calibration shown in fig. 4.6 was performed.

In terms of magnitude, the S_{xx} data shown in Fig. 4.8 is on the same order < 1 μV/K as the Hall bar study by Chickering *et al.* [9] (see Fig. 2.11d) in the vicinity of the 5/2 FQH state. The order of magnitude is surprisingly consistent with eq. (2.13) [6] for non-Abelian quasiparticles in the Hall bar geometry[2]. This could be purely coincidental since the Yang and Halperin prediction of thermopower [6] was derived in the Hall bar geometry. Rather, one would expect the magnitude of S_{xx} in the Corbino geometry to be consistent with the Barlas and Yang theory where $|S_{xx}|$ is expected to saturate to a constant value given by $|S_{xx}(T \to 0)| = \frac{4k_B}{e} \log \sqrt{2} \approx 120$ μV/K, and change sign at the center of the 5/2 FQH state. This is three orders of magnitude larger than what has been observed in our work although our data clearly capture the expected sign change that is unique to the Corbino geometry.

In our experiment, and unfortunately, the energy gap of the 5/2 FQH state was 39(1) mK (see Fig. 4.2) and this is comparable to the electron temperature of $\sim$ 20 mK at which S_{xx} was measured. This implies that the quasiparticles in the 5/2 FQH state are thermally excited from the ground state and are here outside the validity of eq. (2.7) where only the non-Abelian entropy should dominate. Furthermore, we also note that a single ν^* calibration point this was selected to obtain ΔT and was applied to all the data points in Fig. 4.8 regardless of their ν^* locations. As a result and as seen in Fig. 4.9, this may have led to a significant source of inaccuracy in S_{xx}. In order to test the sensitivity of S_{xx} relative to the accuracy of the temperature gradient calibration, the thermovoltage data from Fig. 4.8 was divided by different temperature gradients from calibrations performed at distinct partial filling factors ν^*, and these are shown in Fig. 4.9 color coded. As a result, the inaccuracies in ΔT are significant, leading to a systematic error in the magnitude of S_{xx}, especially further from B_0. Thus, in the future, any attempts in extracting the absolute thermopower S_{xx} should be adequately extracted with a calibration of ΔT at each partial filling factors ν^*.

In addition, we note that a comparison with thermopower data taken in the vicinity of the $\nu = 7/3$ FQH state should be performed as a control experiment in order to provide

---

[2] Taking $d = \sqrt{2}$, $e^* = e/4$, and B=5.18 T, one obtains $S_{xx} \approx 0.4$ μV/K which is close to the $S_{xx} \approx 0.5$ μV/K observed in Fig. 4.8.

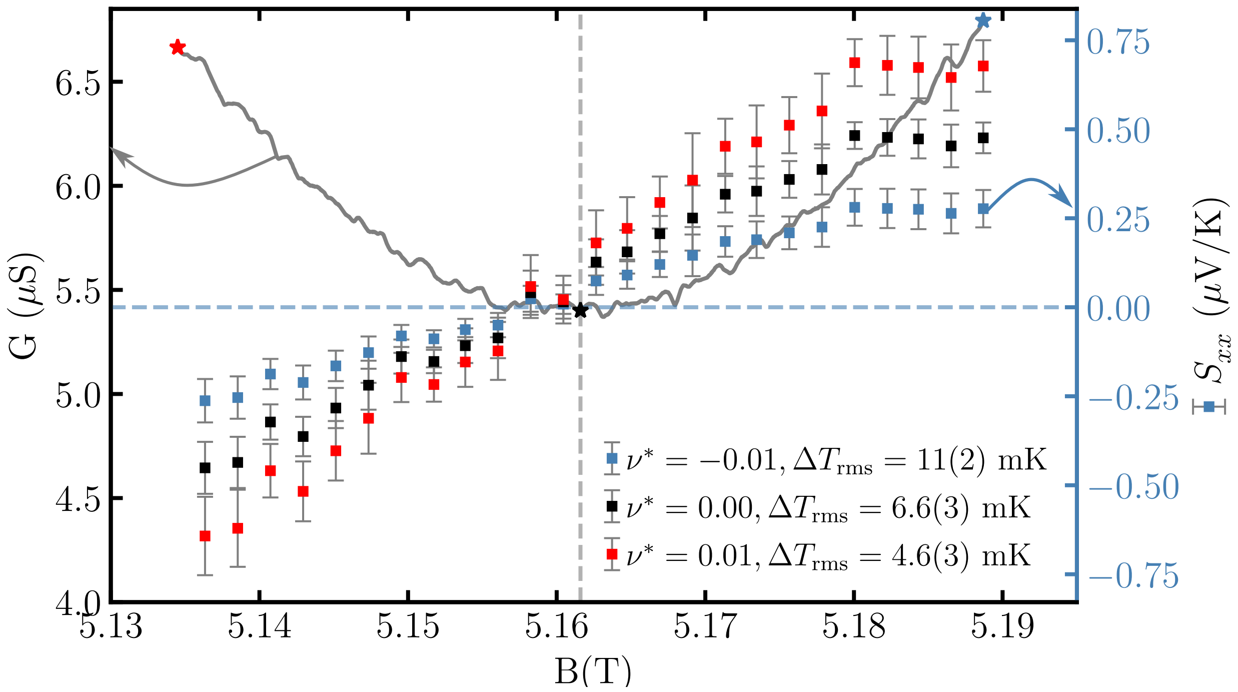

Figure 4.9: Thermopower at $\nu = 5/2$ represented on shared axis with conductance. Each data point is an average over five minutes. The star points indicates where the respective calibrations shown in Fig. 4.6 were performed.

compelling evidence for an interpretation in terms of the non-Abelian entropy predicted by Barlas and Yang [8] (eq. (2.15)). This is because the $\nu = 7/3$ FQH state is expected to be Abelian ($d = 1$) and thus only possess the normal thermodynamic entropy $\mathcal{S}_n(T)$. As such, one would expect to observe a larger thermopower signal at $\nu = 5/2$ than $\nu = 7/3$ in the low-temperature limit where the non-Abelian entropy $\mathcal{S}_d$ dominates over the normal entropy $\mathcal{S}_n(T)$.

Finally, we stress that regardless of the multiple caveats hindering solid interpretation of S_{xx} in terms of its magnitude and (2.15)), a clear sign change was observed and is consistent with the *entropy per quasiparticle per quasiparticle charge* (eq. (2.14)) prediction by Barlas and Yang [8].

4.5 Degradation of the 5/2 state energy gap by the chip resistor heater setup

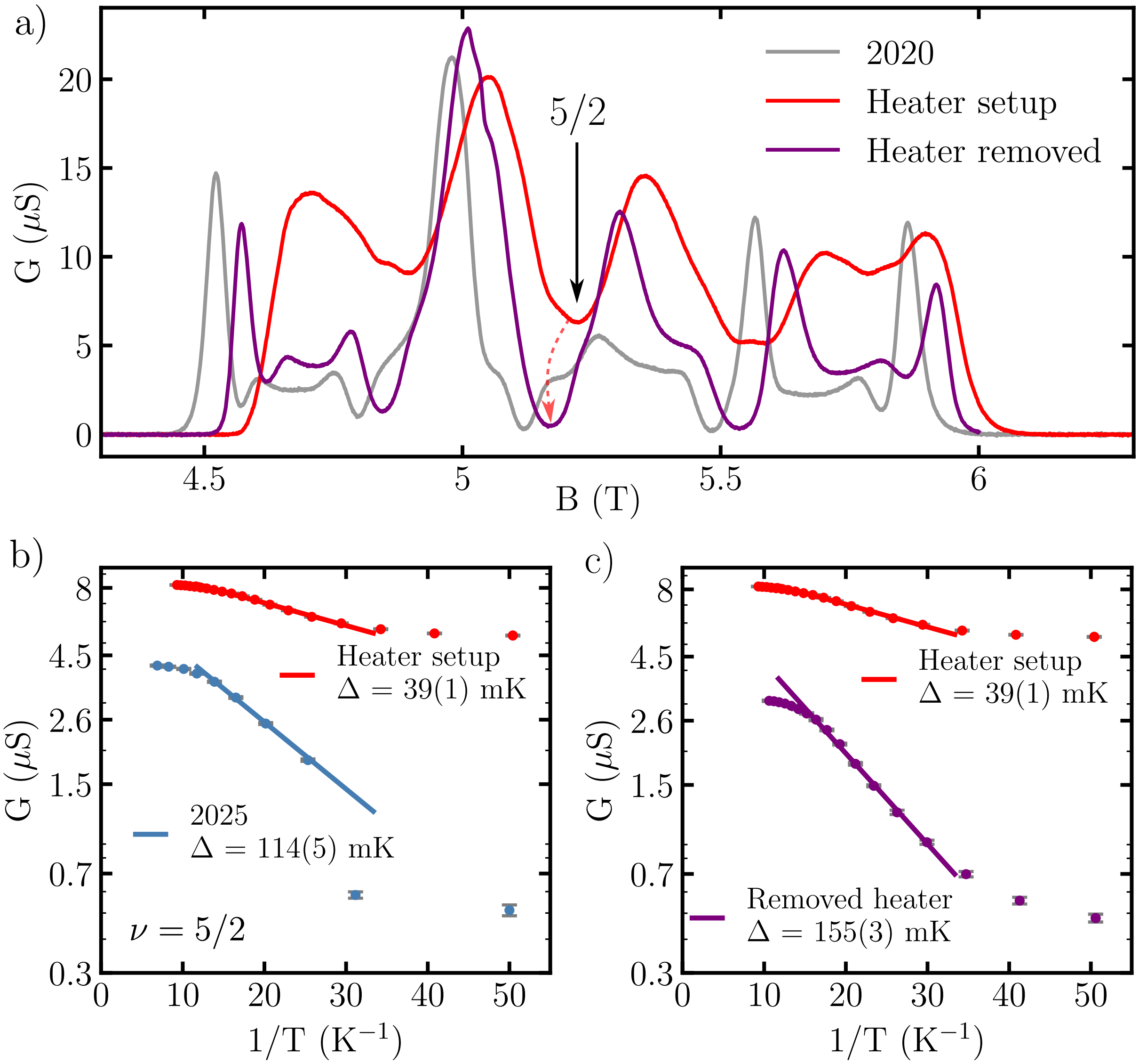

Figure 4.10: a) Electrical conductance as a function of magnetic field in the SLL after removal of the chip resistor heater setup on CB05. b) Energy gap measurement of the $\nu = 5/2$ FQH state with the chip resistor setup on the device. c) Energy gap of the $\nu = 5/2$ FQH state with the chip resistor heater removed from the device.

As stated previously and shown in Fig. 4.2, the installation of the chip resistor setup on the device deteriorated the quality of the 5/2 FQH state to an extent that a clear measurement of non-Abelian entropy was not possible. Fortunately, we believe that this degradation was only coincident with the chip resistor setup being on the device, and not due to an irreversible process. As shown in Fig. 4.10a, upon removal and cleaning[3] of the Corbino device, the electronic transport in the SLL returned to a condition similar to the pristine device, and a sequence of FQH and RIQH states was again clearly observable. Additionally, as shown in Fig. 4.10c, an energy gap of 155(3) mK was measured, which is consistent with what had been measured previously in Fig. 4.2.

There are multiple reasons that could explain such a deterioration of the 5/2 FQH state upon installation of the chip resistor heater setup. The first is that it could have inadvertently introduced a heat source. This could occur if the wiring connected to the heater was not properly heat sunk to the mixing chamber, or if there was a high frequency noise source picked up by the wiring of the heater. These two possibilities were ruled out by installing a heat sink to the mixing chamber as well as a low-pass 1 kHz RC filter in the wiring of the heater, and it resulted in no visible improvement of of the 5/2 FQH energy gap.

Another plausible explanation concerns the adhesive used to glue the chip resistor to the center contact of the Corbino device. This was realized using Apiezon N grease that solidifies at cryogenic temperatures and creates a strong mechanical and thermal bond between the chip resistor and the device. Unfortunately, upon solidification, a mismatch in differential mechanical contraction between the grease and the gold contact may have caused a substantial strain that could have degraded the 5/2 FQH state, as FQH states are known to be highly sensitive to strain [79]. It is however not possible to rule out entirely that the chip resistor itself was responsible for influencing the 5/2 FQH state and further investigations are clearly needed. As next step, one clear improvement would be to mechanically spring load the chip resistor on the contact in a manner analogous to the flip-chip method developed in the Gervais lab [80], rather than relying on an adhesive layer. We note that recently the Gervais lab fabricated a three-terminal device with an electronic mobility in excess of

---

[3] The device was cleaned with sequential trichloroethylene, acetone and methanol baths to remove any trace of Apiezon N grease.

44 cm^2/(Vs) with no apparent degradation of the electron mobility [81]. Thus, we have all reasons to believe that the chip resistor could be mounted in a way that the 5/2 FQH state remains with a large energy gap, leading to entropy measurements that could unravel whether of not a non-Abelian entropy as predicted in the low-temperature limit.

Chapter 5

Conclusion

5.1 Summary

This thesis reports the conception and proof-of-concept for an apparatus designed to probe thermopower in ultra-high mobility GaAs/AlGaAs heterostructures with the ultimate goal of probing non-Abelian entropy in the $\nu = 5/2$ FQH state. Among many possible options, a setup based on a chip resistor heater glued on the center contact of the ultra-high mobility Corbino device was selected for its simplicity and most importantly for providing an excellent thermal contact with the 2DEG, thereby allowing for the usage of a precision quasi-DC lock-in detection technique. Relying on foundational previous works on FQH thermopower in the Hall bar geometry [7, 9, 62], a scheme was devised to induce and measure a temperature gradient in the Corbino annular region. Additionally, a mechanically rigid low-temperature sample stage was designed to mitigate vibrational issues occurring in the BlueFors LD-250 dilution refrigerator where the mK temperature high magnetic field thermoelectric and electronic transport measurements were conducted.

The voltage signals measured with the thermoelectric setup were characterized, and were found to be consistent with Corbino diffusion longitudinal thermopower in the QHE and

FQHE regimes. For instance, we found that S_{xx} vanishes and changes sign at, and in-between LLs. The same behavior was observed in the SLL and was found to be consistent with the quasiparticle and quasihole sign change in the 5/2 FQH state. Then, in order to get an estimate of the entropy, a temperature calibration was performed as a function of partial filling factor ν^*. This calibration was then applied to a measurement of the thermovoltage in close vicinity of the $\nu = 5/2$ FQH state and the magnitude of the thermopower S_{xx} was compared to theoretical predictions of non-Abelian entropy in the Hall bar [6] and Corbino geometries [8]. The order of magnitude of S_{xx} was found to be consistent with a previous experimental work [9] and unexpectedly, it was closer in agreement with the work of Yang and Halperin [6] rather than the Corbino thermopower theory from Barlas and Yang [8]. Subsequent investigations led us to conclude in most likelihood that it was a pure coincidence since the value of S_{xx} was most likely coming from normal entropy since the temperature was close to the measured 5/2 FQH energy gap. In that sense, the reduction of the 5/2 FQH energy gap from 172(5) mK to a mere 39(1) mK likely led to excitation of quasiparticles above its ground state, rendering an interpretation of thermopower as excess non-Abelian dimensional entropy invalid. Nonetheless, of the utmost importance, the observed sign change in S_{xx} was found to be in agreement with the *entropy per quasiparticle per quasiparticle charge* interpretation found by Barlas and Yang, thereby providing compelling evidence for an interpretation of S_{xx} as longitudinal diffusion Corbino thermopower.

5.2 Future outlook

One major improvement for this experiment would be to conceive a new thermoelectric measurement setup that is less invasive and leaves the 2DEG quality pristine. We believe that the current chip resistor heater setup most likely induced strain *via* the adhesive thermally contracting from room to base temperature. Therefore, the thermoelectric setup should be redesigned without relying on any adhesive. As such, a spring-loaded mechanical apparatus with a top piece holding the heater on the contact could be envisioned, and in the advent that a mechanical contact is insufficient, other types of adhesives should be explored. Conversely, a more drastic approach could be attempted, where an entirely new device would be fabricated with an on-chip heater patterned in the center contact.

Upon the 5/2 FQH state degradation having been resolved, it would also be necessary to extend the validity of the temperature gradient calibration by performing it at all the partial filling factors and for each temperature data points where the thermopower data is taken. In addition, this process should be repeated to at least one other FQH state expected to be Abelian such as for the 8/3 or the 7/3 FQH states in order to provide a control experiment. Finally, the parameter space investigated should also span a wider range of temperatures in order to identify distinct entropy regimes, and where clear theoretical predictions exist.

Bibliography

[1] G. E. Moore, Electronics **38**, 1 (1965).

[2] R. Feynman, Int. J. Theor. Phys. **21**, 467 (1982).

[3] P. Shor, Algorithms for quantum computation: discrete logarithms and factoring, in *Proceedings 35th Annual Symposium on Foundations of Computer Science*, pages 124–134, 1994.

[4] M. Kjaergaard, M. E. Schwartz, J. Braumüller, P. Krantz, J. I.-J. Wang, S. Gustavsson, and W. D. Oliver, Annu. Rev. Condens. Matter Phys. **11**, 369 (2020).

[5] C. Nayak, S. H. Simon, A. Stern, M. Freedman, and S. Das Sarma, Rev. Mod. Phys. **80**, 1083 (2008).

[6] K. Yang and B. I. Halperin, Phys. Rev. B **79**, 115317 (2009).

[7] W. Chickering, J. Eisenstein, L. Pfeiffer, and K. West, Phys. Rev. B **81**, 245319 (2010).

[8] Y. Barlas and K. Yang, Phys. Rev. B **85**, 195107 (2012).

[9] W. E. Chickering, J. P. Eisenstein, L. N. Pfeiffer, and K. W. West, Phys. Rev. B **87**, 075302 (2013).

[10] K. von Klitzing, Rev. Mod. Phys. **58**, 519 (1986).

[11] K. S. Novoselov, Z.-f. Jiang, Y.-s. Zhang, S. Morozov, H. L. Störmer, U. Zeitler, J. Maan, G. Boebinger, P. Kim, and A. K. Geim, Science **315**, 1379 (2007).

[12] Y. J. Chung, A. Gupta, K. Baldwin, K. West, M. Shayegan, and L. Pfeiffer, Phys. Rev. B **106**, 075134 (2022).

[13] R. A. Melcer, A. Gil, A. K. Paul, P. Tiwari, V. Umansky, M. Heiblum, Y. Oreg, A. Stern, and E. Berg, Nature **625**, 489 (2024).

[14] B. A. Schmidt, *Specific heat in the fractional quantum Hall regime*, McGill University, 2019.

[15] K. von Klitzing, G. Dorda, and M. Pepper, Phys. Rev. Lett. **45**, 494 (1980).

[16] M. Suddards, A. Baumgartner, M. Henini, and C. J. Mellor, New J. Phys. **14**, 083015 (2012).

[17] D. C. Tsui, H. L. Störmer, and A. C. Gossard, Phys. Rev. Lett. **48** (1982).

[18] H. L. Störmer, Rev. of Mod. Phys. **71**, 875 (1999).

[19] R. B. Laughlin, Phys. Rev. Lett. **50**, 1395 (1983).

[20] F. D. M. Haldane, Phys. Rev. Lett. **51**, 605 (1983).

[21] J. K. Jain, Phys. Rev. Lett. **63** (1989).

[22] B. I. Halperin, P. A. Lee, and N. Read, Phys. Rev. B **47**, 7312 (1993).

[23] L. D. Landau, Sov. Phys. JETP **8**, 70 (1959).

[24] R. Willett, J. P. Eisenstein, H. L. Störmer, D. C. Tsui, A. C. Gossard, and J. H. English, Phys. Rev. Lett. **59**, 1776 (1987).

[25] G. Moore and N. Read, Nucl. Phys. B. **360**, 362 (1991).

[26] M. Greiter, X.-G. Wen, and F. Wilczek, Phys. Rev. Lett. **66**, 3205 (1991).

[27] M. Levin, B. I. Halperin, and B. Rosenow, Phys. Rev. Lett. **99**, 236806 (2007).

[28] S.-S. Lee, S. Ryu, C. Nayak, and M. P. Fisher, Phys. Rev. Lett. **99**, 236807 (2007).

[29] D. T. Son, Phys. Rev. X **5**, 031027 (2015).

[30] K. K. W. Ma, M. R. Peterson, V. W. Scarola, and K. Yang, Fractional quantum hall effect at the filling factor $\nu = 5/2$, in *Encyclopedia of Condensed Matter Physics (Second Edition)*, edited by T. Chakraborty, pages 324–365, Academic Press, Oxford, second edition edition, 2024.

[31] N. Samkharadze, J. Watson, G. Gardner, M. J. Manfra, L. Pfeiffer, K. West, and G. Csáthy, Phys. Rev. B **84**, 121305 (2011).

[32] J. I. A. Li, C. Tan, S. Chen, Y. Zeng, T. Taniguchi, K. Watanabe, J. Hone, and C. R. Dean, Science **358**, 648 (2017).

[33] F. Wilczek, Phys. Rev. Lett. **49**, 957 (1982).

[34] B. I. Halperin, Phys. Rev. Lett. **52**, 1583 (1984).

[35] S. C. Morampudi, A. M. Turner, F. Pollmann, and F. Wilczek, Phys. Rev. Lett. **118**, 227201 (2017).

[36] R. H. Morf, Phys. Rev. Lett. **80**, 1505 (1998).

[37] B. I. Halperin, A. Stern, I. Neder, and B. Rosenow, Phys. Rev. B **83**, 155440 (2011).

[38] C. de C. Chamon, D. E. Freed, S. A. Kivelson, S. L. Sondhi, and X. G. Wen, Phys. Rev. B **55**, 2331 (1997).

[39] J. Nakamura, S. Liang, G. C. Gardner, and M. J. Manfra, Nat. Phys. **16**, 931 (2020).

[40] T. Werkmeister, J. R. Ehrets, M. E. Wesson, D. H. Najafabadi, K. Watanabe, T. Taniguchi, B. I. Halperin, A. Yacoby, and P. Kim, Science **388**, 730 (2025).

[41] N. Read and S. Das Sarma, Nat. Phys. **20**, 381 (2024).

[42] R. L. Willett, K. Shtengel, C. Nayak, L. N. Pfeiffer, Y. J. Chung, M. L. Peabody, K. W. Baldwin, and K. W. West, Phys. Rev. X **13**, 011028 (2023).

[43] J. Kim *et al.*, arXiv:2412.19886 (2024).

[44] M. Dolev, M. Heiblum, V. Umansky, A. Stern, and D. Mahalu, Nature **452**, 829 (2008).

[45] C. L. Kane and M. P. A. Fisher, Phys. Rev. B **55**, 15832 (1997).

[46] M. Banerjee, M. Heiblum, A. Rosenblatt, Y. Oreg, D. E. Feldman, A. Stern, and V. Umansky, Nature **545**, 75 (2017).

[47] S. K. Srivastav, R. Kumar, C. Spånslätt, K. Watanabe, T. Taniguchi, A. D. Mirlin, Y. Gefen, and A. Das, Nat. Commun. **13**, 5185 (2022).

[48] M. Banerjee, M. Heiblum, V. Umansky, D. E. Feldman, Y. Oreg, and A. Stern, Nature **559**, 205 (2018).

[49] B. Dutta, W. Yang, R. Melcer, H. K. Kundu, M. Heiblum, V. Umansky, Y. Oreg, A. Stern, and D. Mross, Science **375**, 193 (2022).

[50] B. Dutta, V. Umansky, M. Banerjee, and M. Heiblum, Science **377**, 1198 (2022).

[51] U. Roy, S. Manna, S. Chakraborty, K. Watanabe, T. Taniguchi, A. Das, M. Goldstein, Y. Gefen, and A. Das, arXiv:2506.12526 (2025).

[52] N. Cooper and A. Stern, Phys. Rev. Lett. **102**, 176807 (2009).

[53] B. Schmidt, K. Bennaceur, S. Bilodeau, G. Gervais, L. Pfeiffer, and K. West, Solid State Commun. **217**, 1 (2015).

[54] B. A. Schmidt, K. Bennaceur, S. Gaucher, G. Gervais, L. N. Pfeiffer, and K. W. West, Phys. Rev. B **95**, 201306 (2017).

[55] M. Petrescu, Z. Berkson-Korenberg, S. Vijayakrishnan, K. West, L. Pfeiffer, and G. Gervais, Nat. Commun. **14**, 7250 (2023).

[56] H. J. Goldsmid *et al.*, *Introduction to thermoelectricity*, Springer, 2010.

[57] H. Ibach and H. Lüth, *Solid-state physics: an introduction to principles of materials science*, Springer Science & Business Media, 2013.

[58] N. Cooper, B. Halperin, and I. Ruzin, Phys. Rev. B **55**, 2344 (1997).

[59] M. Carrega, D. Ferraro, A. Braggio, N. Magnoli, and M. Sassetti, Phys. Rev. Lett. **107**, 145404 (2011).

[60] R. Shirasaki, A. Endo, N. Hatano, and H. Nakamura, J. Electron. Mater. **41**, 1540 (2012).

[61] M. Jonson and S. Girvin, Phys. Rev. B **29**, 1939 (1984).

[62] W. E. Chickering, *Thermopower in two-dimensional electron Systems*, California Institute of Technology, 2016.

[63] N. Sultana, R. W. Rienstra, K. Watanabe, T. Taniguchi, J. A. Stroscio, N. B. Zhitenev, D. E. Feldman, and F. Ghahari, Nat. Phys. **21**, 724 (2025).

[64] N. d'Ambrumenil and R. Morf, Phys. Rev. Lett. **111**, 136805 (2013).

[65] H. Van Zalinge, R. Van der Heijden, and J. Wolter, Phys. Rev. B **67**, 165311 (2003).

[66] S. Kobayakawa, A. Endo, and Y. Iye, J. Phys. Soc. Jpn. **82**, 053702 (2013).

[67] M. A. Real, D. Gresta, C. Reichl, J. Weis, A. Tonina, P. Giudici, L. Arrachea, W. Wegscheider, and W. Dietsche, Phys. Rev. Appl. **14**, 034019 (2020).

[68] M. A. Real, A. Tonina, L. Arrachea, P. Giudici, C. Reichl, W. Wegscheider, and W. Dietsche, Appl. Phys. Lett. **122**, 103101 (2023).

[69] J. M. Herrera, M. A. Real, C. Reichl, A. Tonina, W. Wegscheider, W. Dietsche, and L. Arrachea, Phys. Rev. B **103**, 125404 (2021).

[70] X. Liu, T. Li, P. Zhang, L. N. Pfeiffer, K. W. West, C. Zhang, and R.-R. Du, Phys. Rev. B **97**, 245425 (2018).

[71] F. Poitevin, *Bias Spectroscopy of Coulomb Drag Between Vertically Integrated Quantum Wires*, McGill University, 2025.

[72] F. Pobell, *Matter and methods at low temperatures*, volume 2, Springer, 2007.

[73] H. Wang, F. Yang, Y. Guo, K. Peng, D. Wang, W. Chu, and S. Zheng, Measurement **131**, 204 (2019).

[74] F. Boivin, M. Petrescu, Z. Berkson-Korenberg, L. N. Pfeiffer, K. W. West, and G. Gervais, arXiv:2509.09588 (2025).

[75] B. I. Halperin and J. K. Jain, *Fractional quantum hall effects: new developments*, World Scientific, 2020.

[76] C. R. Dean, B. A. Piot, P. Hayden, S. Das Sarma, G. Gervais, L. N. Pfeiffer, and K. W. West, Phys. Rev Lett. **101**, 186806 (2008).

[77] A. M. Chang, M. A. Paalanen, D. C. Tsui, H. L. Störmer, and J. C. M. Hwang, Phys. Rev. B **28**, 6133 (1983).

[78] R. A. Melcer, A. Gil, A. K. Paul, P. Tiwari, V. Umansky, M. Heiblum, Y. Oreg, A. Stern, and E. Berg, Nature **625**, 489 (2024).

[79] S. P. Koduvayur, Y. Lyanda-Geller, S. Khlebnikov, G. Csáthy, M. J. Manfra, L. N. Pfeiffer, K. W. West, and L. P. Rokhinson, Phys. Rev. Lett. **106**, 016804 (2011).

[80] K. Bennaceur, B. A. Schmidt, S. Gaucher, D. Laroche, M. P. Lilly, J. L. Reno, K. W. West, L. N. Pfeiffer, and G. Gervais, Sci. Rep. **5**, 13494 (2015).

[81] T. Martz-Oberlander, B. Bulgaru, Z. Berkson-Korenberg, K. W. West, L. N. Pfeiffer, and G. Gervais, in preparation. (2025).

[82] J. B. Johnson, Phys. Rev. **32**, 97 (1928).

Appendix A

Device radiation shielding

The device was encapsulated in a OFHC copper RF box to shield out unwanted thermal and electromagnetic radiation as shown in Fig. A.1. A custom made G10 post was machined to hold the device at the field center as shown in Fig. A.1b.

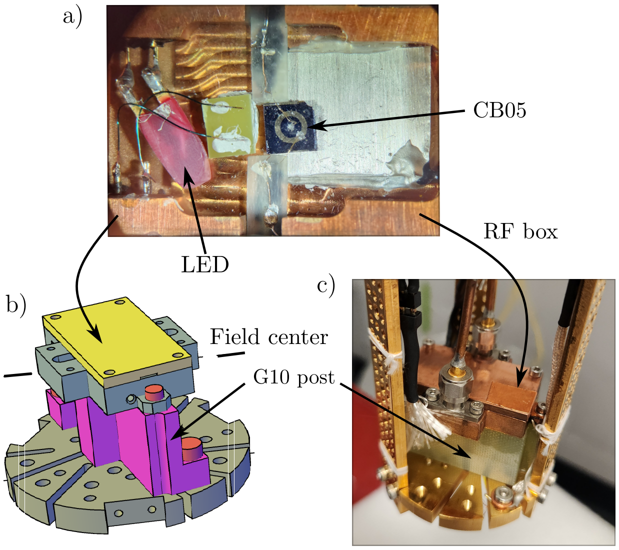

Figure A.1: a) Image of the thermoelectric experiment showing the Corbino device, the LED and the wiring of the chip resistor heater. Note that the chip resistor is too small to be visible on this image but is contained within the center contact of the device. b) Drawings of the RF box, G10 post, and slotted bottom plate. c) Image of the assembly on the sample stage.

Appendix B

Derivation of the relationship between the thermal gradient and the average temperature of the 2DEG

To model the heat flow in the Corbino device, the heat equation in polar coordinates is modified by removing the θ dependence since the temperature profile is expected to be uniform in θ. The result is shown in eq. (B.1)

$$c\frac{\partial T}{\partial t} = \kappa \frac{1}{r}\frac{\partial}{\partial r}\left(r\frac{\partial T}{\partial r}\right), \tag{B.1}$$

where c is the specific heat of the 2DEG and κ is its thermal conductance. It is assumed that both quantities are constant on the range of temperature considered even though κ and c are temperature dependent. This assumption is reasonably respected since the temperature gradients ΔT are expected to be less than 35% of the base temperature T_0. In our system, the temperature is fixed by the cryostat at $r = r_2$ and a heating power $\dot{Q}$ is introduced at

$r = r_1$, leading to boundary conditions given by

$$\Delta T(r_2) = 0 \quad \text{and} \quad \left.\frac{\partial T}{\partial r}\right|_{r_1} = -\frac{\dot{Q}}{\kappa}.$$

Solving eq. (B.1) in steady state and accounting for the boundary conditions, a logarithmic temperature profile is obtained

$$\Delta T(r) = \frac{r_1 \dot{Q}}{\kappa} \log \frac{r_2}{r}. \tag{B.2}$$

Experimentally, we only have access to the relation between $\dot{Q}$ and $\langle T \rangle$ which is given by the temperature dependence of the conductance $G(T)$. We can integrate eq. (B.2) to compute the average temperature in the 2DEG

$$\langle T \rangle = \frac{1}{r_2 - r_1} \int_{r_1}^{r_2} T(r) dr = T_0 + \frac{r_1 \dot{Q}}{\kappa} \left(1 - \frac{r_1 \log \frac{r_2}{r_1}}{r_2 - r_1} \right).$$

Combining this result with eq. (B.2), we get that the relation between ΔT and the experimentally accessible average temperature $\langle T \rangle - T_0$ is given by

$$\Delta T = \frac{\langle T \rangle - T_0}{1 - \frac{r_1 \log \frac{r_2}{r_1}}{r_2 - r_1}} = 1.86 \left(\langle T \rangle - T_0 \right). \tag{B.3}$$

Appendix C

Thermopower setup electrical validations

Table C.1 lists the two-point resistances between all the components of the device and chip resistor heater setup.

Table C.1: Two point resistances in the thermoelectric Corbino setup

T	300 K	7 mK
Contact pair	R	R
CB05 IN OUT	810 Ω	292 Ω
H+ H-	200 Ω	374 Ω
H+ IN	>50 MΩ	>10 MΩ
H- IN	>50 MΩ	>10 MΩ
H+ OUT	>50 MΩ	>10 MΩ
H- OUT	>50 MΩ	>10 MΩ

There is no evidence for a short between one of the heater contacts to the device (CB05) inner contact (IN) as all the H+, H-, IN and OUT pairs show an immeasurably large resistance. The increase in resistance observed in the chip resistor heater at low temperature is expected for ruthenium oxide chip resistors.

In Fig. C.1, the data from Fig. 4.3c is represented here as a function of I_{heat}^2 in order to show the agreement with the expected Joule heating of the chip resistor. As observed in this figure, the conductance is linear with respect to I_{heat}^2 except in the low-power region of the negative $-I_{\mathrm{heat}}$ branch. This is the case because the $-I_{\mathrm{heat}}$ data was not acquired after sufficient thermal relaxation time from the data run in the I_{heat} branch, meaning that the average temperature of the 2DEG was not at base temperature, but still in the process of cooling down.

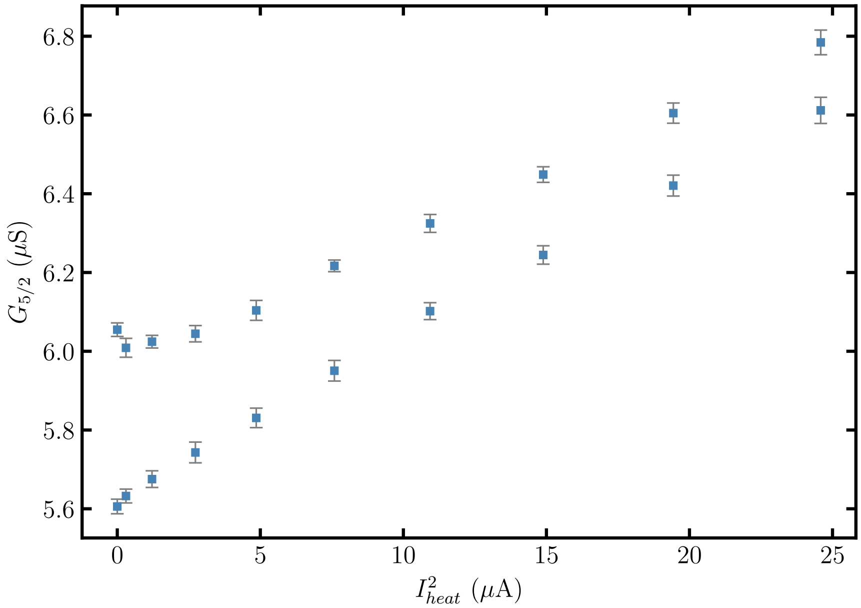

Figure C.1: Conductance at 5/2 as a function of the current squared I_{heat}^2.

Appendix D

Preliminary thermopower results in an non-ideal in-plane field

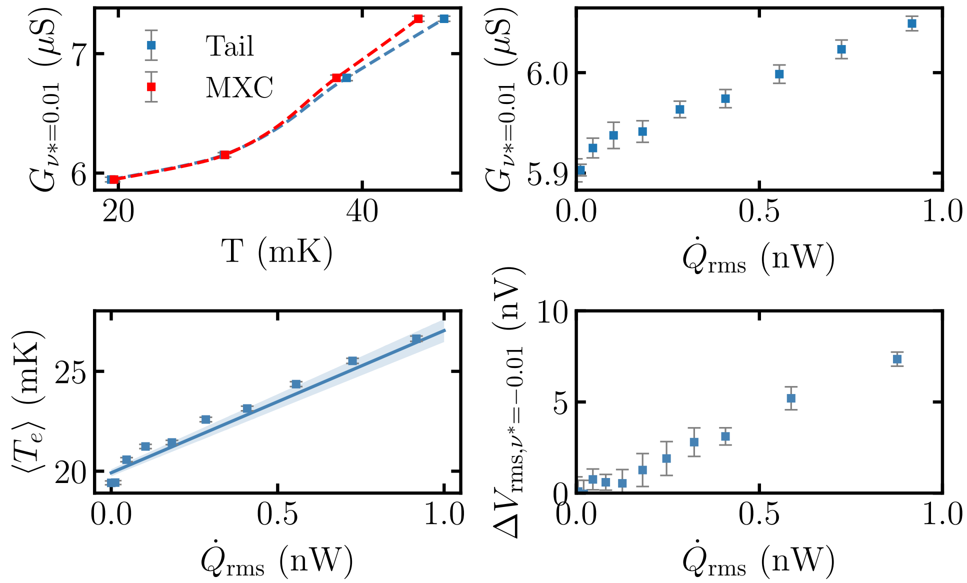

Figure D.1: Temperature calibration at $\nu* = 0.01$. **a)** Conductance versus temperature in the vicinity of the 5/2 at $\nu* = 0.01$ (B = 5.1852 T). An interpolation is performed and shown as a dashed line. **b)** Conductance versus RMS heater power at the same filling factor. **c)** Average temperature of the 2DEG versus RMS heater power. The solid blue line is a linear fit. **d)** RMS thermovoltage as a function of RMS heating power.

Appendix E

Investigation of the uncertainty and noise in the thermopower signal

The dominant source of uncertainty in the error bars of Fig. 4.9 is the RMS voltage noise of around 0.4 nV which is significant compared to thermovoltage signals of below 2 nV, especially close to $\nu^* = 0$. This 0.4 nV voltage noise translates to 4.5 $\mathrm{nV_{rms}}/\sqrt{\mathrm{Hz}} = 6.4$ $\mathrm{nV}/\sqrt{\mathrm{Hz}}$ when the bandwidth of the lock-in is considered[1] and is close to the 4 $\mathrm{nV}/\sqrt{\mathrm{Hz}}$ input voltage noise of the SR560 pre-amplifier. However, there is still room for improvement by selecting a pre-amplifier with even lower input noise. Additionally, the Johnson–Nyquist noise [82], shown with a black dashed line in Figs. E.1b and E.2b, is around 0.3 $\mathrm{nV}/\sqrt{\mathrm{Hz}}$ at 10 mK and for the $\sim$ 200 kΩ impedance device. On the other hand, in terms of precision and accuracy, the thermovoltage ΔV_{rms} is currently the dominant source of imprecision on the thermopower S_{xx} while the dominant parameter affecting the exactitude of the measurement is ΔT_{rms}. The 0.4 $\mathrm{nV_{rms}}$ thermovoltage noise on a 2 nV signal yields a relative error of 20% which is dominant over the 6% relative error on ΔT_{rms}. Alternatively, based on the results of Fig. 4.9, ΔT_{rms} influences the exact value of S_{xx}, especially if the dependence with ν^* is

---

[1] The noise bandwidth Δf of the lock-in is given by $\Delta f = \frac{5}{64 t_c}$ where t_c is the time constant of the 24 dB roll-off averaging filter.

not considered.

Moreover, the precision on both quantities can be improved with more averaging and longer time constants on the SR830 lock-in amplifier. The current time constant is 10 s for the thermovoltage measurement and 3 s for the conductance circuit, which ultimately defines the uncertainty on the temperature gradient. To improve the exactitude of ΔT_{rms}, one needs to characterize it at every partial filling factor ν^* where a thermovoltage data point is recorded. Each individual calibration could be also improved with more data points containing less uncertainty in the $G(T)$ and $G(\dot{Q}_{\mathrm{rms}})$ curves. In this work, some optimization of the thermovoltage noise was performed but was limited to characterizing the effect of the measurement time constant t_c, frequency f, pre-amplifier bandwidth Δf and pre-amplifier gain g.

The time constant t_c of the SR830 lock-in amplifier was incremented until $t_c = 10$ s and an improvement of the signal to noise ratio (SNR) was observed for each increment. However, a maximum of 10 s was employed to get a reasonable acquisition time for this earlier investigation of S_{xx}, but t_c can be increased significantly to reduce the effect of noise provided that acquisition time is not a defining factor. The effect of lock-in detection frequency f on the thermovoltage and its noise was also investigated for frequencies below 90 Hz as shown in Fig. E.1, which is approximately 20 times lower than the limit set by the $\tau \sim 0.5$ ms thermal response time of the chip resistor heater. Nevertheless, as seen in Fig. E.1a, a noticeable phase shift appearing as a signal in the X channel of the lock-in amplifier begins to occur for frequencies roughly above 50 Hz. This means that one must probe a frequency at least 40 times larger than the thermal response time limit in order to avoid unphysical phase shifts in the thermovoltage signal. In contrast, the noise gets reduced as the frequency is increased since f gets further away from the $1/f$ noise regime. Hence, there is an optimization process to select the most appropriate frequency based on these two constraints as illustrated by the shaded regions in Fig. E.1. As a result, a frequency of 37.78

Hz was selected, also taking into account that harmonics of common frequencies such as 60 Hz must be avoided.

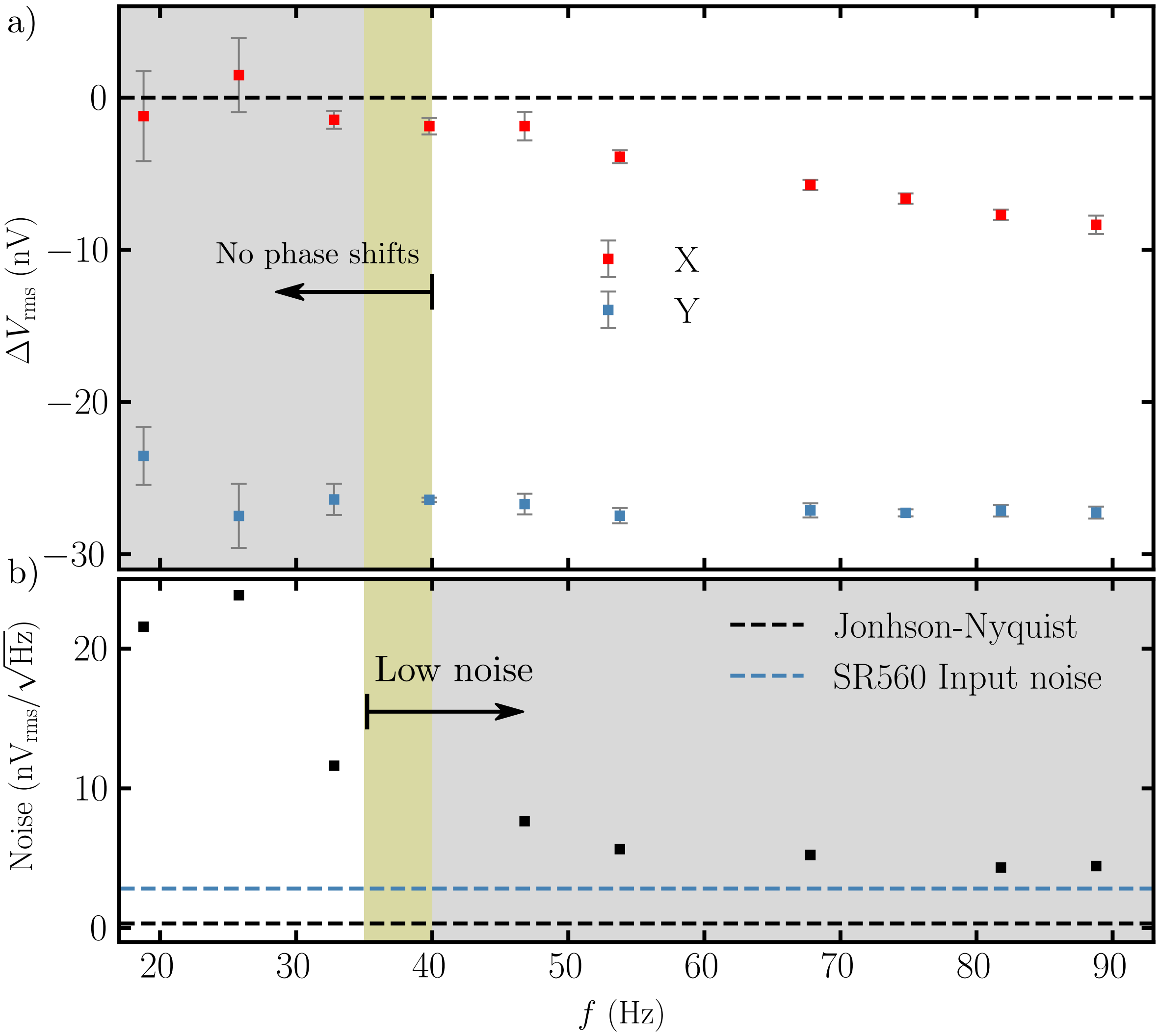

Figure E.1: Optimization of the lock-in detection frequency. a) Voltage detected in the X and Y channels of the SR830 lock-in as a function of frequency. b) Noise in the thermovoltage (Y channel) versus frequency compared to the Jonhson-Nyquist noise and the SR560 input noise.

The SR560 pre-amplifier parameters were also optimized in terms of bandwidth and gain. As a first note, the bandwidth of the thermovoltage measurement circuit as shown in Fig. 3.5a is ultimately only determined by the bandwidth defined by the SR830 lock-in time constant, *e.g.* for $t_c = 10$ s, the bandwidth is ~ 8 mHz and is always much smaller than the bandwidth available on the SR560. However, it can still be useful to filter the noise at unwanted frequencies before amplification. As such, no effect on the SNR was found by reducing the bandwidth but it was still chosen to be as small as possible around $f = 37.78$ Hz without distorting the signal, *i.e.* 0.1 Hz to 10 kHz. In contrast to the SR560 pre-amplifier bandwidth, the gain has a significant effect on the SNR as shown in Fig. E.2. Two circuit configurations were tested, one where the SR560 was placed on the instrument rack with $\sim$ 3 m long coaxial cables connecting it to the cryostat wiring and one where the SR560 was connected with $\sim$ 10 cm long coaxial cables and placed on top of the cryostat. It turned out that the *instrument rack* configuration yielded a better SNR in opposition to what one would expect when reducing the length of the leads. Nevertheless, as indicated by a circle in Fig. E.2, the optimal gain is consistently found to be 500 regardless of the SR560 circuit layout.

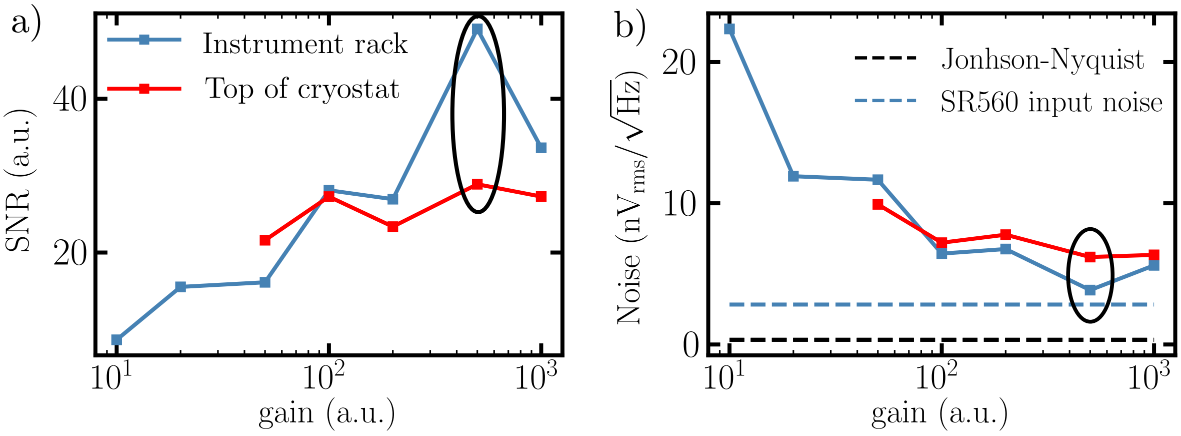

Figure E.2: Optimization of the SR560 pre-amplifier gain where the optimal gain is circled and consistent for both configurations. a) SNR as a function of the SR560 gain. b) Voltage noise versus SR560 gain.